Preprint Title	Tuning the photophysical property of naphthalimide-phenothiazine dyads by variation of the electron donating and accepting capability: synthesis and study of the intersystem crossing and thermally-activated delayed fluorescence
Authors	Liyuan Cao, Xi Liu, Xue Zhang, Jianzhang Zhao, Fabiao Yu and Yan Wan
Publication Date	25 Apr. 2023
Article Type	Full Research Paper
Supporting Information File 1	Supporting Information.docx; 14.6 MB
ORCID® iDs	Liyuan Cao - https://orcid.org/0000-0001-8701-8585; Xue Zhang - https://orcid.org/0000-0003-3681-202X

Tuning the photophysical property of naphthalimide-phenothiazine dyads by variation of the electron donating and accepting capability: synthesis and study of the intersystem crossing and thermally-activated delayed fluorescence

Liyuan Cao‡[1], Xi Liu‡[2], Xue Zhang‡[1], Jianzhang Zhao*[1], Fabiao Yu*[3] and Yan Wan*[2]

[1]State Key Laboratory of Fine Chemicals, Frontier Science Center for Smart Materials, School of Chemical Engineering, Dalian University of Technology, 2 Ling Gong Road, Dalian, 116024, P. R. China.

[2]College of Chemistry, Beijing Normal University, Beijing 100875, P. R. China.

[3]Key Laboratory of Hainan Trauma and Disaster Rescue, The First Affiliated Hospital of Hainan Medical University, Hainan Medical University, Haikou 571199, P. R. China.

Email:

Jianzhang Zhao* - zhaojzh@dlut.edu.cn

Yan Wan* - wanyan@bnu.edu.cn

Fabiao Yu* - yufabiao@hainmc.edu.cn

Notes:

The authors declare no competing financial interest.

* Corresponding author

‡ Equal contributors

Abstract

A series of naphthalimide (NI)-phenothiazine (PTZ) electron donor-acceptor dyads were prepared to study the thermally activated delayed fluorescence (TADF) property of the dyads, from a point of view of detection of the various transient species. The photophysical properties of the dyads were tuned by changing the electron donating and the electron withdrawal capability of the PTZ and NI moieties, respectively, by oxidation of the PTZ unit, or by using different arylamines to attach with the NI unit. This tuning effect was manifested in the UV–vis absorption and fluorescence emission spectra, e.g., the change of the charge transfer absorption bands. TADF was observed for the dyads containing native PTZ unit, and the prompt and delayed fluorescence lifetimes changed when different arylamine was used. In polar solvent, no TADF was observed. For the dyads with the PTZ unit oxidized, no TADF was observed as while. Femtosecond transient absorption spectra show that the charge separation takes ca. 0.6 ps, and admixture of locally excited (^{3}LE) state and charge separated (^{1}CS/^{3}CS) states formed (in *n*-hexane). The subsequent charge recombination from the ^{1}CS state takes ca. 7.92 ns. Upon oxidation of the PTZ unit, the beginning of charge separation is at 178 fs, and formation of ^{3}LE state takes 4.53 ns. Nanosecond transient absorption (ns-TA) spectra show that both ^{3}CS and ^{3}LE states were observed for the dyads showing TADF, whereas only ^{3}LE or ^{3}CS state was observed for the systems lacking of TADF. This is a rare but unambiguous experimental evidence that the spin-vibronic coupling of ^{3}CS/ ^{3}LE states is crucial for TADF. Without the mediating effect of the ^{3}LE state, no TADF is resulted, even the long-lived ^{3}CS state is populated (lifetime $\tau_{CS} \approx$ 140 ns). This experimental result confirms the $^3\text{CS} \rightarrow {}^1$CS reverse intersystem crossing (rISC) is slow, without coupling with an approximate ^{3}LE state. These studies are useful for in-depth understanding of the photophysical mechanisms of the TADF emitters, as

well as for molecular structure design of new electron donor-acceptor TADF emitters.

Keywords

Charge-transfer; Electron donor; Intersystem crossing; TADF; Triplet state

Introduction

Thermally activated delayed fluorescence (TADF) compounds are promising emitters to be used in organic light-emitting diode (OLED) [1-12]. These emitters have the advantage of low cost, high harvesting efficiency of both the singlet and triplet excitons, thus high quantum efficiency for the electroluminescence [13]. The TADF emission process involves the reverse intersystem crossing (rISC) from the triplet (T_1) state to the emissive singlet (S_1) state. A typical molecular structure motif for this kind of emitters is electron donor-acceptor dyad, and the molecular geometry is usually orthogonal, i.e., the planes of the π-conjugation system of the electron donor and acceptor is perpendicular to each other. As a result, the HOMO and LUMO are spatially separated. This molecular geometry is beneficial to reduce the S_1/T_1 states energy gap, makes the rISC possible. Because of the orthogonal molecular orbitals, the electron exchange energy (J) of the two unpaired electrons is small, which leads to small S_1/T_1 states energy gap ($2J$). Moreover, the orthogonal geometry is beneficial for the intersystem crossing (ISC) of the dyads, i.e., via the spin orbit charge transfer ISC (SOCT-ISC) [14-18]. It can be considered as a generalization of the El-Sayed's rule for ISC. This SOCT-ISC may also enhance the rISC in OLED devices, in which the electron-hole recombination produces mainly the triplet state (the theoretical probability is 75%, by following the spin statistic rule) [1].

Compared to the application studies, the investigation of the photophysical mechanism of TADF emitters is far from mature [19-21]. Initially two-state model was used for understanding of the photophysical processes of the electron donor-acceptor TADF emitters [9, 22-26]. Soon it was realized this over simplified model is non-sufficient. For instance, the singlet/triplet charge separated states ^{1}CS and ^{3}CS of these emitters are believed to undergo non-efficient, slow interconversion, thus the poor rISC will not lead to efficient TADF. Later, three-state model was proposed, i.e., the ^{1}CS, ^{3}CS and a locally excited (^{3}LE) state should be involved in the TADF processes, the rISC is facilitated by the ^{3}LE state, which share similar energy with the ^{3}CS state, e.g., the so-called spin-vibronic coupling effect, as a result, the rISC is fast and efficient, significant TADF can be resulted [13,27-31]. It was also proposed that vibration facilitates the ISC in the TADF emitters [32,33]. However, the most popular optical spectroscopic methods previously used in this area, such as the very often used transient photoluminescence spectral measurement, or the luminescence lifetime measurement, is unable to defect the dark states of the TADF emitters, i.e., the ^{3}LE and ^{3}CS state. Femtosecond transient absorption spectroscopy (fs-TA) was rarely used for the study of the photophysics of the TADF emitters [12,34-37], however, it suffers from the limitation of the time window of detection (up to a few ns). Nanosecond transient absorption spectra were used for study of the TADF mechanisms [38-44], but the examples are limited. Recently, time-resolved electron paramagnetic resonance (TREPR) spectroscopy was used for study of the photophysical mechanisms of the TADF emitters [33, 39, 44-46]. However, the examples are rare. Therefore, much room is left for study of the photophysical mechanism of the TADF emitters, especially to find experimental evidence of the spin-vibronic coupling effect, i.e., the involvement of the dark states, such as ^{3}LE and ^{3}CS states, in the TADF process of the electron donor-acceptor emitters.

In order to address the above challenge, herein we prepared a series of electron donor-acceptor dyads, based on naphthalimide (NI) electron acceptor, and phenothiazine (PTZ) electron donor. The two units are connected by a C–N single bond, and they adopt orthogonal geometry due to the conformation restriction. In order to tune the excited states energy, and to probe the effect of the energy ordering of the transient species involved in the TADF photophysical process, the electron donating strength of the PTZ moiety is reduced by oxidation of the sulfur atom to a sulfoxide structure. Conversely, the electron accepting capability of the NI unit is varied by using different arylamines, which contain electron donating and withdrawal moieties. Although we reported NI-PTZ analogous dyads recently, the fs-TA spectroscopy was not used, and the molecular structures are different from the current dyads [47]. The photophysical processes of dyads were studied with steady state UV–vis absorption spectra, transient photoluminescence spectra, nanosecond/femtosecond transient absorption spectra, electrochemistry, as well as DFT / TDDFT computations. We observed experimental evidence for the spin vibronic coupling effect in the TADF photophysical processes of the electron donor-acceptor emitters.

Results and discussion

Molecular design and structure confirmation

PTZ is a commonly used electron donor with strong electron donating ability (E_{OX} = +0.18 V, vs. Fc/Fc^+) [48], while the NI chromophore is an electron acceptor (E_{RED} = –1.72 V, vs. Fc/Fc^+) [49]. NI and PTZ units are directly connected by a C–N single bond, which makes the π-conjugation plane of the NI and PTZ units adopting perpendicular geometry (Scheme 1). This is beneficial for SOCT-ISC. Previously we

Scheme 1. Synthesis of the Compounds[a].

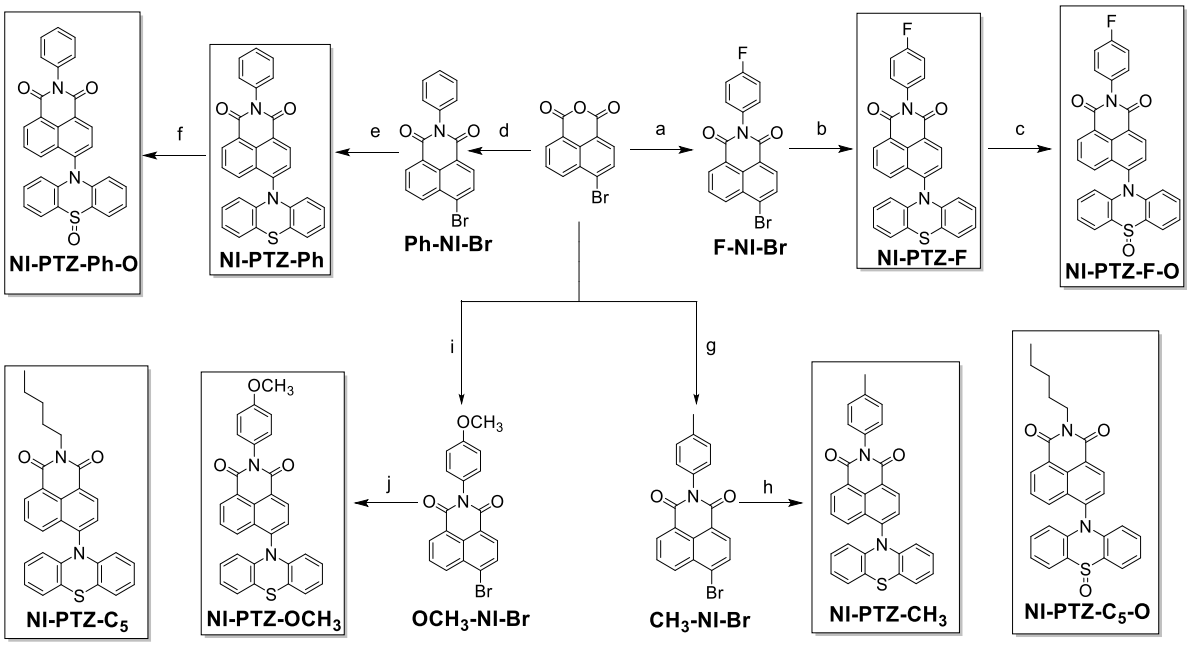

[a] Key: (a) 4-fluoroaniline, acetic acid, N_2, reflux, 7 h, yield: 72%; (b) phenothiazine sodium *tert*-butoxide, dry toluene, tri-*tert*-butylphosphine tetrafluoroborate, $Pd(OAc)_2$, 120 °C ,8 h, yield: 15%; (c) H_2O_2 (30%), CH_3COOH, 40 °C, 1 h, yield: 76%; (d) aniline, acetic acid, N_2, reflux, 7 h; yield: 89%; (e) similar to step (b), yield: 52%; (f) similar to step (c), yield: 82%; (g) *p*-toluidine, acetic acid, N_2, reflux, 7 h, yield: 83%; (h) similar to step (b), yield: 80%; (i) *p*-anisidine, acetic acid, N_2, reflux, 7 h, yield: 75%; (j) similar to step (b), yield: 22%.

observed TADF with an analogue of **NI-PTZ-C$_5$** (the difference of the molecular structures is the alkyl chain, we called that analogue NI-PTZ-N here) [39]. In order to study the effect of tuning the excited states energy, and the ordering of the excited states, on the photophysical property of the dyad, especially the ISC and TADF property, we introduced electron donating and withdrawal arylamine on the NI unit (**NI-PTZ-F**, **NI-PTZ-Ph**, **NI-PTZ-CH$_3$**, **NI-PTZ-OCH$_3$**), and the electron donating ability of the PTZ unit was achieved by oxidation of the unit to sulfoxide (**NI-PTZ-F-O**, **NI-PTZ-Ph-O**, **NI-PTZ-C$_5$-O**). The advantage of such change to oxidation approach is that almost only the ^{1}CS and ^{3}CS states energy are changed, while the other factors are kept intact to large extent [46,50]. For instance, the LE state, the electron exchange energy (*J*) for the unpaired electrons of the CS states (^{1}CS/^{3}CS state energy gap is

2*J*), the ^{1}LE/^{3}LE states energy gap of the NI moiety are all not changed by the unique molecular structure modification method [51]. This approach is useful for studying of molecules showing complicated, entangled photophysical processes upon photoexcitation, for instance the electron donor-acceptor type of TADF emitters [44,46]. Recently we reported NI-PTZ analogous dyads, however, the molecular structures are different from the current dyads, and the photophysical property was tuned by variation of the distance between the NI and the PTZ units, or by oxidation of the PTZ unit [47]. In the current dyads, we used different strategies.

The syntheses of the dyads are based on the known derivatization chemistry of NI and PTZ chromophores, which use Buchwald–Hartwig coupling reaction (Another **NI-PTZ** paper) [39]. The oxidation of the PTZ unit was readily performed by using H_2O_2 as oxidant (Scheme 1). All the compounds were obtained by satisfactory fields, and the molecular structures were fully characterized by ^{1}H NMR, ^{13}C NMR and HRMS spectra (Experimental section).

UV–vis absorption and fluorescence emission spectra

The UV–vis absorption spectra of the compounds are studied (Figures 1 and S27 in Supporting Information File 1). For the compounds without oxidation of the PTZ unit, there are characteristic absorption bands in the 300–350 nm range, which is attributed to the NI moiety, i.e., originated from $S_0 \rightarrow {}^1$LE transition (Figure 1a). Moreover, in the range of 375–570 nm, there is a weak, broad absorption band centered at 460 nm, which is assigned to the $S_0 \rightarrow {}^1$CS transition [52-54], it is similar to the analogue of NI-PTZ-C_5 [39]. In addition, as the aniline attached on the NI unit changed from electron-pulling groups to electron-pushing groups, the absorption peak of the CS is blue-shifted and the absorbance decreases (Figures S28 in Supporting Information File 1). For the

oxidized molecules, the CS absorption peak blue shifts to 360–420 nm range (Figure 1b). These results indicate that upon oxidation of the PTZ unit, the electronic coupling between the donor and acceptor is reduced [55].

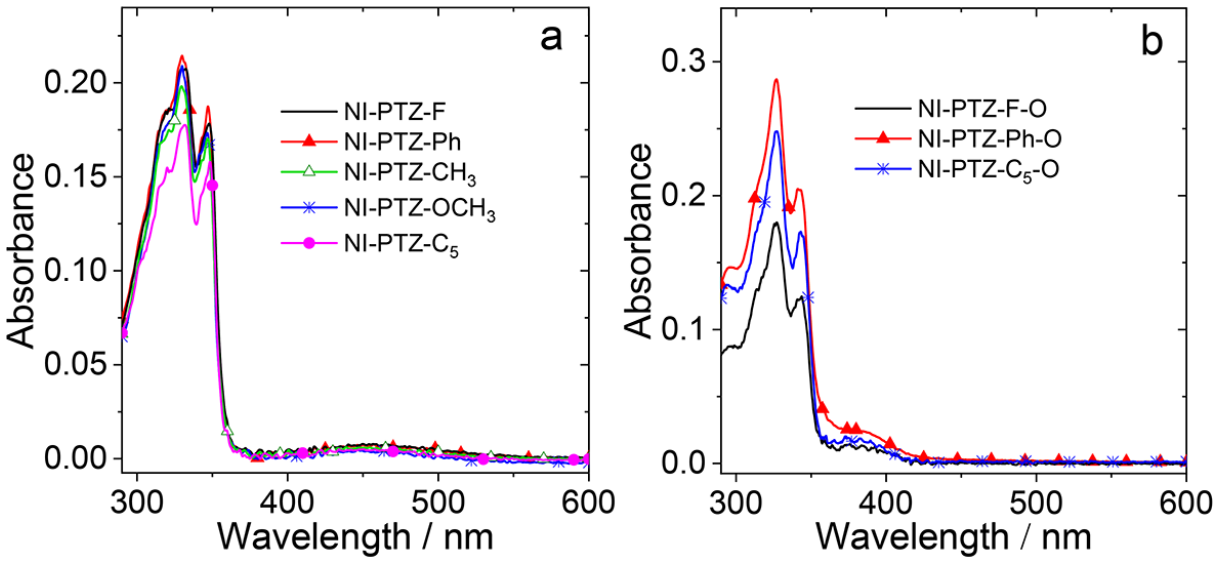

Figure 1: UV−vis absorption spectra of (a) **NI-PTZ-F**; **NI-PTZ-Ph**; **NI-PTZ-CH$_3$**; **NI-PTZ-OCH$_3$**; **NI-PTZ-C$_5$** and (b) **NI-PTZ-F-O**; **NI-PTZ-Ph-O**; **NI-PTZ-C$_5$-O** in *n*-hexane (HEX), $c = 1.0 \times 10^{-5}$ M, 20 °C.

The fluorescence spectra of the compounds are studied (Figures 2 and S29 in Supporting Information File 1). For the compounds with native PTZ unit, like **NI-PTZ-F**, there are broad, structureless fluorescence bands centered at ca. 620 nm in cyclohexane (CHX) and HEX, which are attributed to the CS state emission. Moreover, the fluorescence of the compounds is strongly quenched and red-shifted in polar solvents, as compared to that in CHX and HEX. The higher polarity solvents can stabilize the CS state, and the energy of CS state will decrease, as a result, the emission band will be red-shifted and the fluorescence intensity will be greatly reduced. The results are infer that the emissive S_1 state has substantial CS character [56]. Thus, assignment of the emissive S_1 state to a CS state is reasonable.

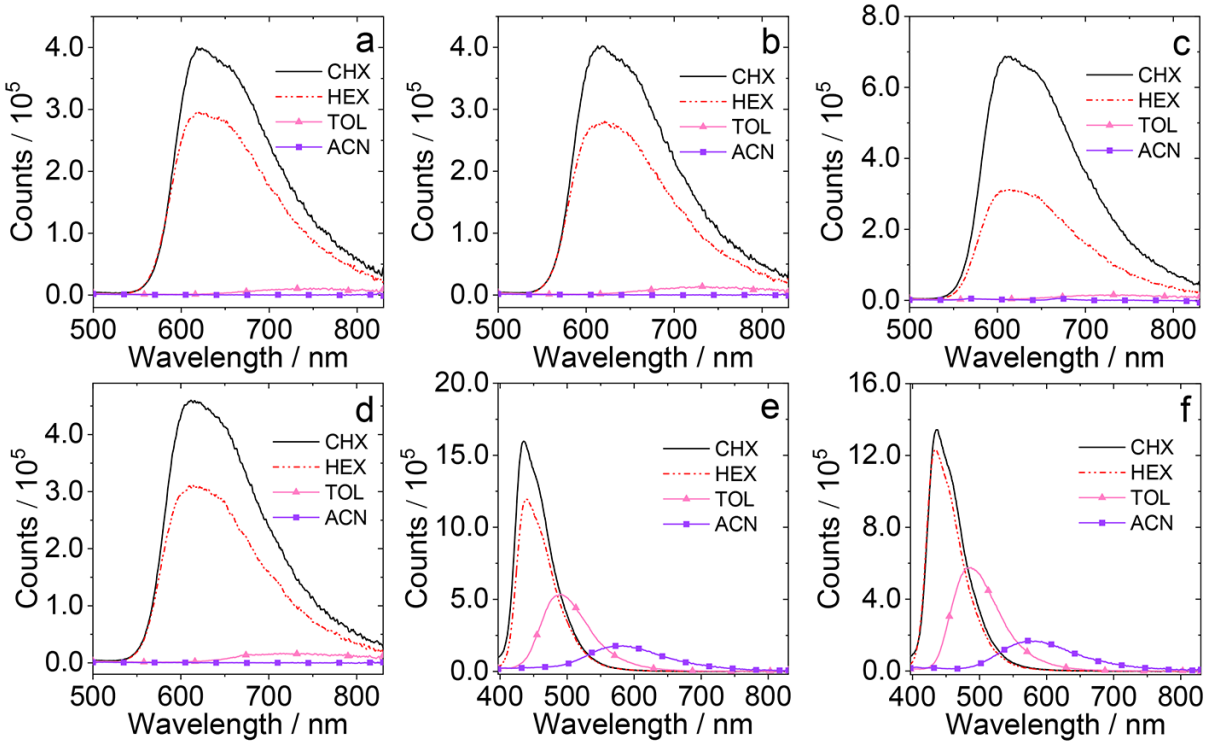

Figure 2: Fluorescence spectra of the dyads. (a) **NI-PTZ-F**; (b) **NI-PTZ-Ph**; (c) **NI-PTZ-CH$_3$**; (d) **NI-PTZ-OCH$_3$**; (e) **NI-PTZ-F-O** and (f) **NI-PTZ-Ph-O** different solvents. The solvents used are: CHX, HEX, toluene (TOL) and acetonitrile (ACN). Optically-matched solutions were used, A = 0.107, λ_{ex} = 310 nm, 20 °C.

Upon oxidation of the PTZ moiety, the degree of fluorescence quenching in polar solvents become less significant than that of the compounds with native PTZ unit (Figure 2e, 2f) [57]. Moreover, note the CS emission wavelength of **NI-PTZ-F-O** and **NI-PTZ-Ph-O** is different from the 4-diphenylamine NI [58]. These results indicate the ^{1}CS state of these two dyads involves the oxidized PTZ unit, as a whole of electron donor, not only the N atom of the PTZ unit [59,60]. Note, the **NI-PTZ-F-O** and **NI-PTZ-Ph-O** adopt orthogonal geometry, and the N atom in PTZ unit is not in π-conjugation with NI moiety, due to conformation restriction [55]. Thus, it is not the ordinary intramolecular charge transfer (ICT) state that affect the fluorescence of these two dyads, indeed, the highly solvent polarity dependent fluorescence emission, intensity

and wavelength are different from the 4-amino NI derivatives, which are much less solvent polarity-dependent [59,61].

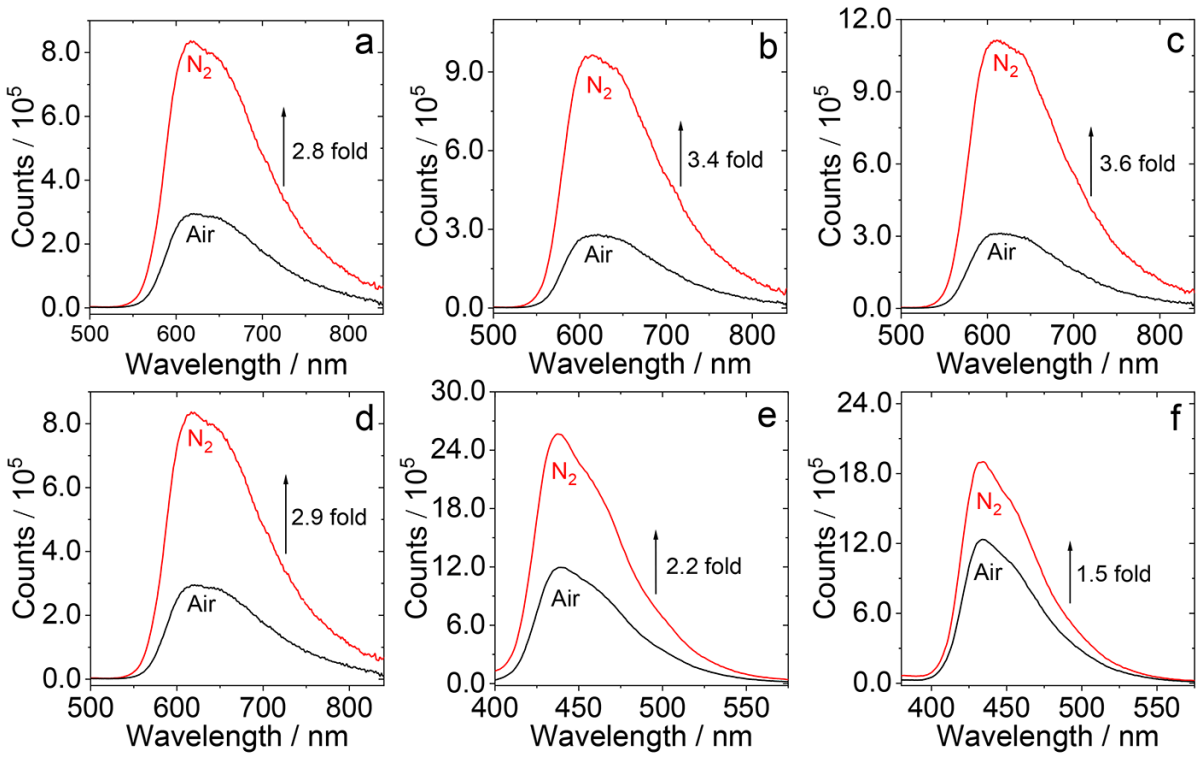

Figure 3: Fluorescence spectra of the dyads. (a) **NI-PTZ-F**; (b) **NI-PTZ-Ph**; (c) **NI-PTZ-CH$_3$**; (d) **NI-PTZ-OCH$_3$**; (e) **NI-PTZ-F-O** and (f) **NI-PTZ-Ph-O** in HEX under different atmospheres (N_2, Air). Optically-matched solutions were used, A = 0.107, λ_{ex} = 310 nm, 20 °C.

Since TADF molecule is characterized by stronger fluorescence under nitrogen atmosphere and substantial quenching under air or oxygen atmosphere [22], the fluorescence spectra of the dyads containing native PTZ unit under different atmospheres are studied (Figure 3a-d and Figure S30a in Supporting Information File 1). The results show that the fluorescence intensity of the dyads is stronger under N_2 atmosphere, but is significantly quenched under air atmosphere. The fluorescence intensity under N_2 atmosphere is 2–4 folds higher than that under air atmosphere.

However, for the dyads with PTZ oxidized (Figure 3e, f and Figure S30b in Supporting Information File 1), the fluorescence intensity is less dependent on the atmosphere. Moreover, we suggest that the reduced luminescence of oxidized molecules in air may be caused by the quenching of oxygen to the S_1 state. According to this experimental phenomenon, we preliminarily speculate that the dyads with native PTZ unit may have TADF property, but not for the oxidized molecule.

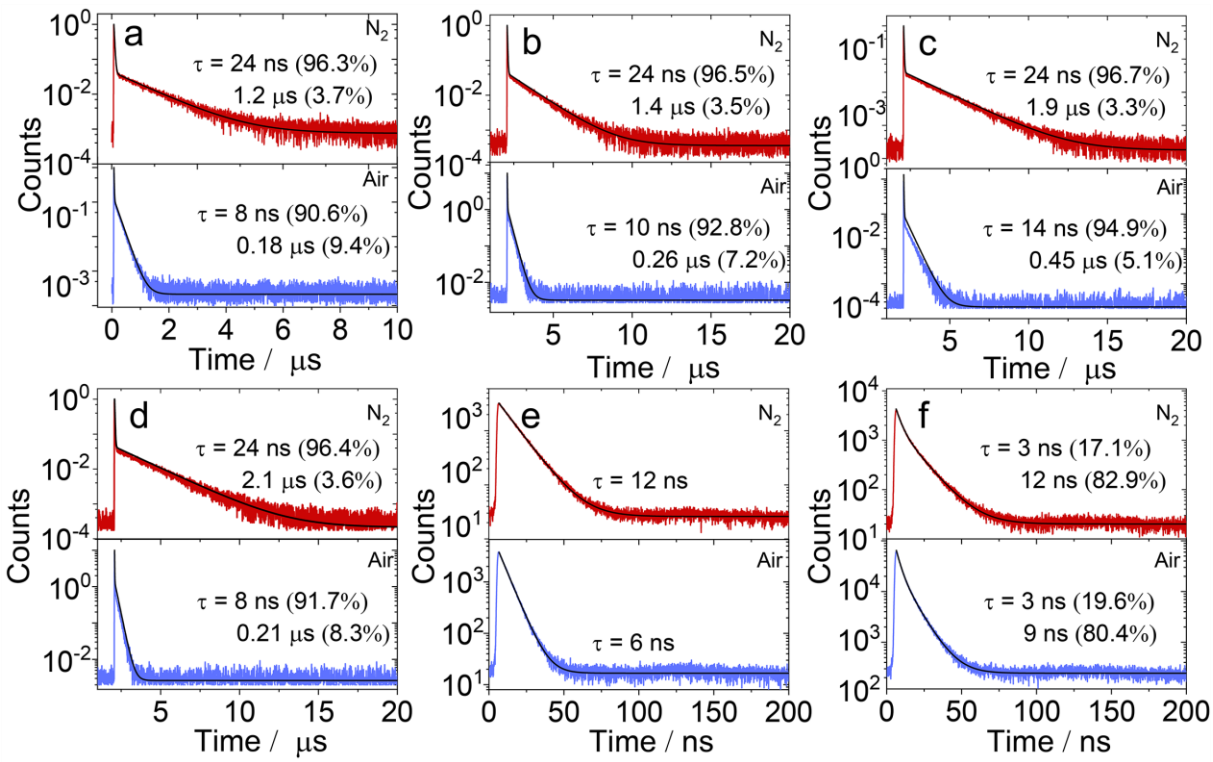

Figure 4: Fluorescence lifetime of (a) **NI-PTZ-F**; (b) **NI-PTZ-Ph**; (c) **NI-PTZ-CH$_3$**; (d) **NI-PTZ-OCH$_3$** (λ_{em} = 610 nm, c = 1.0 × 10^{-5} M) and (e) **NI-PTZ-F-O**; (f) **NI-PTZ-Ph-O** (λ_{em} = 440 nm, c = 2.0 × 10^{-5} M) in different atmosphere (N_2, Air). Excited with picoseconds pulsed laser (λ_{ex} = 340 nm), in HEX, 20 °C.

To confirm the above speculation, the fluorescence decay traces of the dyads are studied in detail (Figure 4 and S31 in Supporting Information File 1). The fluorescence lifetime decay traces of the dyads containing native PTZ unit in HEX show an obvious

double exponential feature. For example, the lifetime of **NI-PTZ-F** is 24 ns (96.3%)/1.2 μs (3.7%) under N_2 atmosphere (Figure 4a). The short-lived component can be attributed to the prompt fluorescence of $^1CS \rightarrow S_0$, while the long-lived component is the delayed fluorescence, via the rISC process. In addition, the lifetime of the long-lived component of the compound under air atmosphere is greatly shortened, which also verifies that these compounds have the property of TADF. Moreover, with our derivatization approach, the geometry and electron donating ability of the PTZ unit are unchanged, but the electron accepting ability of NI part is changed by introducing different arylamines (Figure 4a-4d), we found the magnitude of the long-lived components of TADF emitters is changed. Interestingly, the dyads with the PTZ unit oxidized do not have long-lived components (Figure 4e, 4f), and their fluorescence lifetimes are basically the same in nitrogen and air atmosphere, and the lifetimes are on nanosecond scale, indicating that the oxidized molecules do not have TADF properties. We reported NI-PTZ analogous dyads recently, however, the delayed fluorescence lifetimes are much longer (2.0−14.4 μs) as compared to the current dyads [47]. TADF emitters with shorter delayed fluorescence lifetimes are suitable for frication of OLED devices, to suppress the efficiency roll-off effect.

The photophysical data of all compounds are compiled in Table 1. The fluorescence quantum yields (Φ_F) of the compounds were measured with optical integration sphere, Φ_F values are in the range of 2−7% for the dyads with PTZ unoxidized and oxidized. It is interesting to note that the fluorescence quantum yields of the dyads are low, which are similar to the native NI (Φ_F = 0.5% in HEX), but much lower than 4-diphenylamine NI (Φ_F = 75% in HEX) [58]. We propose there is an efficient non-radiative decay channel for the S_1 state of these dyads, especially for the dyads with the PTZ unit oxidized. ISC is one possible relaxation pathway, because the orthogonal geometry of

the dyads is beneficial for SOCT-ISC. Previously we have shown that SOCT-ISC occurs for the analogue of NI-PTZ-C_5 [39].

Table 1. Photophysical Parameters of the Compounds.

Compounds	λ_{abs}(nm)[a]	ε[b]	λ_{em}(nm)[c]	τ_F(ns)[d]	Φ_F (%)[e]	k_r[f]	k_{nr}[g]
NI-PTZ-F	333	2.1	620	8 (90.6%)	3.5	3.9	1.2
				180 (9.4%)		0.01	0.06
NI-PTZ-Ph	330	2.1	619	10 (92.8%)	3.5	3.2	1.0
				260 (7.2%)		0.01	0.04
NI-PTZ-CH_3	329	2.0	611	14 (94.9%)	3.5	2.4	0.7
				450 (5.1%)		0.0	0.02
NI-PTZ-OCH_3	330	2.1	611	8 (91.7%)	4.1	4.7	1.2
				210 (8.3%)		0.02	0.05
NI-PTZ-C_5	332	1.8	611	9 (94.4%)	2.6	2.7	1.1
				240 (5.6%)		0.01	0.04
NI-PTZ-F-O	329	2.0	440	6	3.5	5.8	1.6
NI-PTZ-Ph-O	330	2.1	434	3 (19.6%)	4.1	2.7	3.3
				9 (80.4%)		3.7	1.1
NI-PTZ-C_5-O	332	1.8	433	6	2.6	4.3	1.6

[a]Maximal UV–vis absorption wavelength in HEX, c =1.0 × 10^{-5} M, 20 °C; [b]Molar absorption coefficient at absorption maxima in HEX,ε: 10^4 M^{-1} cm^{-1}; [c]Emission wavelength in HEX; [d]Fluorescence lifetime under air atmosphere, in HEX, λ_{ex} = 340 nm; [e]Fluorescence quantum yields determined in HEX, λ_{ex} = 310 nm; [f]Radiative decay rate constant. $k_r = \Phi_F / \tau_F$, in 10^6 s^{-1}; [g]Nonradiative decay rate constant. $k_r = (1-\Phi_F) / \tau_F$, in 10^8 s^{-1}.

In order to study the ISC efficiency of the dyads, we measured the singlet oxygen quantum yield (Φ_Δ) of the dyads in solvents with varying polarity (Table 2). For the dyads containing unoxidized PTZ, the Φ_Δ is less than 20% in low polar solvents, and Φ_Δ become negligible in polar solvents. It should be noted that given the lowest transient species was not ^{3}LE state, instead a CS state, no formation of $^1O_2$ should be observed (Figure 7, Figure S33 and S34 in Supporting Information File 1). For the dyads with the PTZ unit oxidized, however, the Φ_Δ are much higher, especially in polar solvents. These results indicate that the lowest state of these dyads is ^{3}LE stats, and the ISC yields are close to unit (Figure 8 and S35 in Supporting Information File 1).

However, these results do not necessarily mean that the ISC of the dyads containing native PTZ unit is poor, it can be the lowest transient state of these dyads is a CS state. We confirmed this is the case for the dyads of **NI-PTZ-F**, etc.

Table 2. Singlet Oxygen Quantum Yields (Φ_Δ. In%) in Different Solvents[a].

Compounds	CHX	HEX	TOL	DCM	ACN
NI-PTZ-F	12	18	0	–[b]	–[b]
NI-PTZ-Ph	14	18	1	–[b]	–[b]
NI-PTZ-CH_3	15	17	0	–[b]	–[b]
NI-PTZ-OCH_3	14	23	2	–[b]	–[b]
NI-PTZ-C_5	17	19	1	–[b]	–[b]
NI-PTZ-F-O	25	30	50	100	100
NI-PTZ-Ph-O	23	26	46	100	90
NI-PTZ-C_5-O	28	36	48	100	96

[a]The E_T (30) values of the solvents are 30.9 (CHX), 31.0 (HEX), 33.9 (TOL), 40.7 (DCM) and 45.6 (ACN), respectively, in kcal mol^{-1}. Singlet oxygen quantum yield (Φ_Δ) with $Ru(bpy)_3[PF_6]_2$ as standard (Φ_Δ = 0.57 in DCM) in different solvents, λ_{ex} = 340 nm; [b]Not observed.

Electrochemistry study

In order to obtain the energy of the CS state, The electrochemistry of these compounds was studied (Figure 5). A reversible oxidation wave at +0.29 V (vs. Fc/Fc^+) was observed for **NI-PTZ-F**, which is attributed to the oxidation of the PTZ part. Moreover, a reversible reduction wave was observed at the –1.78 V (vs. Fc/Fc^+) due to the reduction of NI unit. For all the dyads containing native PTZ unit, the oxidation potentials are virtually the same, however, the reduction potential changed to some

extent, which is consistent with our molecular design to keep the donor part unchanged and change NI part by introducing different electron pushing and withdrawal arylamines groups. For **NI-PTZ-F-O**, an irreversible oxidation wave at +1.38 V (vs. Fc/Fc^+) was observed, which may due to the weak electron donating ability of the PTZ part after oxidation, and there was still a reversible reduction potential at −1.53 V (vs. Fc/Fc^+). Slightly catholically shifted reduction waves were observed for other dyads containing oxidized PTZ unit, **NI-PTZ-Ph-O** and **NI-PTZ-C_5-O**.

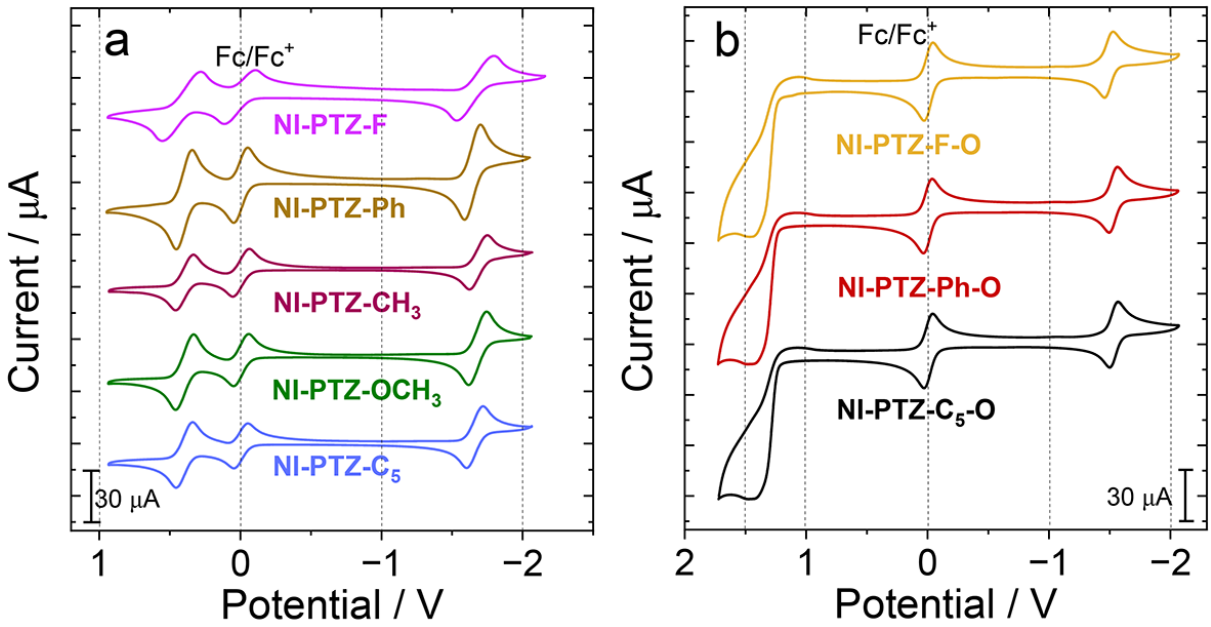

Figure 5: Cyclic voltammogram of the compounds. (a) **NI-PTZ-F**; **NI-PTZ-Ph**; **NI-PTZ-CH_3**; **NI-PTZ-OCH_3**; **NI-PTZ-C_5** in deaerated DCM and (b) **NI-PTZ-F-O**; **NI-PTZ-Ph-O**; **NI-PTZ-C_5-O** in deaerated ACN. Ferrocene (Fc) was used as internal reference (set as 0 V in the cyclic voltammograms). 0.10 M Bu_4NPF_6 as supporting electrolytes. Scan rates: 100 mV/s, c = 1.0 × 10^{-3} M, 20 °C.

The redox potentials of the compounds were presented in Table 3. And the Gibbs free energy changes (ΔG_{CS}) for charge separation (CS) as well as the energy of the charge

transfer states (E_{CS}) were calculated using the Rhem–Weller equation (*E*qs. 1-3) and the obtained values are listed in Table 4 [62-64].

$$\Delta G_{CS} = e(E_{OX} - E_{RED}) - E_{00} + \Delta G_S \quad (1)$$

$$\Delta G_S = -\frac{e^2}{4\pi\varepsilon_S\varepsilon_0 R_{CC}} - \frac{e^2}{8\pi\varepsilon_0}\left(\frac{1}{R_D} + \frac{1}{R_A}\right)\left(\frac{1}{\varepsilon_{REF}} - \frac{1}{\varepsilon_S}\right) \quad (2)$$

$$E_{CS} = e[E_{OX} - E_{RED}] + \Delta G_S \quad (3)$$

Table 3: Electrochemical Redox Potentials of the Compounds[a].

Compounds	$E_{(OX)}$/V	$E_{(RED)}$/V
NI-PTZ-F[b]	+0.29	−1.78
NI-PTZ-Ph[b]	+0.35	−1.69
NI-PTZ-CH$_3$[b]	+0.33	−1.75
NI-PTZ-OCH$_3$[b]	+0.33	−1.74
NI-PTZ-C$_5$[b]	+0.34	−1.72
NI-PTZ-F-O[c]	+1.38	−1.53
NI-PTZ-Ph-O[c]	+1.38	−1.56
NI-PTZ-C$_5$-O[c]	+1.37	−1.56

[a]Cyclic voltammetry in N_2-saturated solvents containing 0.10 M Bu_4NPF_6. Pt electrode as the counter electrode, glassy carbon electrode as the work electrode, Ferrocene (Fc/Fc^+) as the internal reference (set as 0 V in the cyclic voltammograms), and $Ag/AgNO_3$ couple as the reference electrode; [b]Measured in DCM; [c]Measured in ACN.

It should be noted that the E_{00} values used in the analysis is the S_1 state energy, not the T_1 energy, because we have shown that the CS is fast in this kind of compact dyads, and the precursor of the CS is ^{1}LE state [58]. From Table 4, it is found that the ΔG_{CS} of these compounds are negative in all solvents, indicating that the charge separation process is thermodynamically allowed in these solvents. And the CS state energy of

dyads calculated by the redox potentials are slightly higher than the experimental values in HEX (the fluorescence, Figure 2). For the unoxidized molecules, with increasing the solvent polarity, the CS state energy decrease sharply. From HEX to ACN, the CS state energy level decrease by ca. 0.7 eV. Note we did not determine the electron exchange energy (*J*) concerning the unpaired electrons in the CS state (^{1}CS/^{3}CS states energy gap is 2*J*). However, since the dyads takes orthogonal geometry, the ^{1}CS/^{3}CS states energy gap should be small, on $<$ 0.1 eV scale [39, 58]. For the dyads with PTZ moiety oxidized, the CS state energy is higher than that of unoxidized molecules, and it is also decreased with increasing the solvent polarity.

Table 4. Gibbs Free Energy Changes of the Charge Separation (ΔG_{CS}) and Charge Separation States Energy (E_{CS}) of the Compounds[a].

Compounds	ΔG_{CS} (eV)				E_{CS} (eV)			
	HEX	TOL	DCM	ACN	HEX	TOL	DCM	ACN
NI-PTZ-F[b]	−0.23	−0.39	−0.83	−0.95	2.38	2.22	1.78	1.66
NI-PTZ-Ph[c]	−0.26	−0.42	−0.86	−0.98	2.35	2.19	1.75	1.63
NI-PTZ-CH$_3$[d]	−0.29	−0.40	−0.84	−0.96	2.34	2.23	1.79	1.67
NI-PTZ-OCH$_3$[e]	−0.25	−0.41	−0.85	−0.97	2.37	2.21	1.78	1.66
NI-PTZ-C$_5$[f]	−0.26	−0.41	−0.86	−0.98	2.37	2.21	1.77	1.65
NI-PTZ-F-O[g]	−0.02	−0.18	−0.63	−0.75	3.22	3.06	2.62	2.49
NI-PTZ-Ph-O[h]	−0.01	−0.17	−0.62	−0.74	3.25	3.06	2.65	2.52
NI-PTZ-C$_5$-O[i]	−0.02	−0.18	−0.63	−0.75	3.24	3.08	2.64	2.51

[a]Cyclic voltammetry in deaerated solutions containing a 0.10 M Bu_4NPF_6. Pt electrode is counter electrode, glassy carbon electrode is working electrode, and $Ag/AgNO_3$ couple as the reference electrode; [b]E_{00} = 2.61 eV; [c]E_{00} = 2.61 eV; [d]E_{00} = 2.63 eV; [e]E_{00} = 2.63 eV; [f]E_{00} = 2.62 eV; [g]E_{00} = 3.24 eV; [h]E_{00} = 3.26 eV; [i]E_{00} = 3.26 eV. E_{00} (E_{00} = 1240/λ) is the singlet state energy of compounds, λ is the wavelength of the crossing point of normalized UV−vis absorption spectra and fluorescence emission spectra.

The T_1 state of NI was determined as 2.25 eV (by phosphorescence method) [65], and the T_1 state of PTZ unit was determined as 2.45 eV (phosphorescence method) [66]. These energy levels are close to the CS states (Table 4), thus, in HEX and TOL, the three state ^{1}CS, ^{3}CS, ^{3}LE share similar energy, TADF may be resulted. For the dyads with the PTZ unit oxidized, the E_{CS} state of the **NI-PTZ-F-O**, **NI-PTZ-Ph-O** and **NI-PTZ-C_5-O** was increased for ca. 0.8 eV. Thus, we do not expect TADF for these three dyads, especially in HEX. In polar solvents, such as ACN, no TADF was observed.

Femtosecond transient absorption (fs-TA) spectra

In order to study the charge separation (CS), charge recombination (CR) and ISC of the compounds, the femtosecond transient spectra were studied (Figure 6). Taking the **NI-PTZ-F** as an example, the transient absorption spectra measured in HEX and the evolution associated difference spectra (EADS), obtained by global fitting based on sequential kinetic model, are presented (Figure 6a, 6b). The first transient species (black line in Figure 6b) is attributed to a localized singlet excited state of ^{1}NI* by comparison with the reported spectra of NI [58]. Within 155 fs, the system evolves to the second spectrum (blue line), for which both a sharp peak centered at 404 nm and a broad band in the range 600−750 nm were observed, which is identified as a relaxation of the ^{1}NI* state and the evolution towards a CS state. Then within about 599 fs, the system evolves to the third spectrum, which shows a sharp absorption band centered at 433 nm and 522 nm, these are the absorption of $NI^{-\bullet}$ and $PTZ^{+\bullet}$, thus it is due to a CS state. Then within 12.84 ps, another spectrum is developed, which is still the characteristic of CS state, however, the intensity of the two bands increases and both peaks blue shifts by about 3 nm, indicating a vibrational relaxation of the charge separated (CS) state, thus we propose the geometry and solvent relaxation takes ca. 12.84 ps. At the same time, in this process, the triplet features of ^{3}LE start to appear

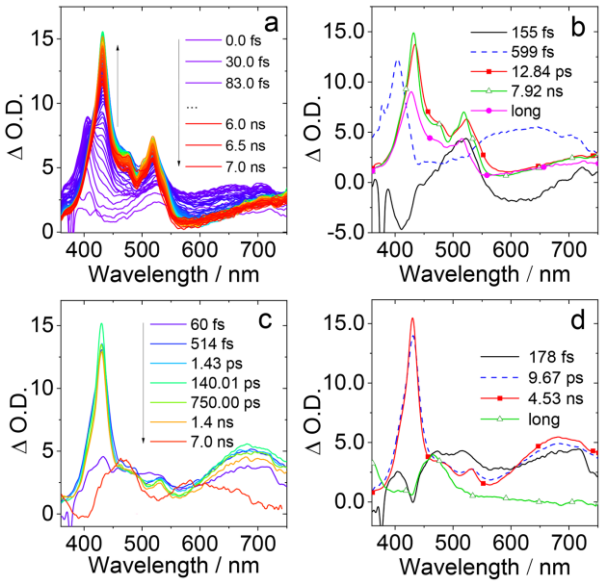

Figure 6: Femtosecond transient absorption spectra of **NI-PTZ-F**. (a) Transient absorption spectra and (b) the EADS obtained with global analysis in HEX. Femtosecond transient absorption spectra of **NI-PTZ-F-O** (c) Transient absorption spectra; (d) relative EADS obtained with global analysis in ACN. λ_{ex} = 340 nm.

(460 nm). Since the relaxed CS state and CR evolve within 7.92 ns, this is in agreement with the TADF luminescence studies (ca. 8 ns, Figure 4a), thus the decay of the ^{1}CS state in aerated solution takes ca. 7.92 ns. Then the system evolves to the final spectrum (magenta), which is characterized with the features of ^{3}LE and CS states, and it is in good agreement with the ns-TA results (Figure 7a). Moreover, we propose that the precursor of ^{3}CS state is ^{3}LE state. While in ACN (Figure S32a and S32b in Supporting Information File 1), the fluorescence lifetime is not observed, we speculate that the ^{1}CS $\rightarrow$ ^{3}LE $\rightarrow$ ^{3}CS process is very fast, and within 8.08 ps, a ^{3}LE state has been formed and quickly relaxed to ^{3}CS state, with some characteristic absorption peaks of $NI^{-\bullet}$ (430 nm) and $PTZ^{+\bullet}$ (502 nm). This process is too fast to detect the ^{3}LE state, and finally we only see the ^{3}CS state. This is an experimental evidence for the spin-vibronic coupling model of the TADF mechanism. Although we reported NI-PTZ

analogous dyads recently, the fs-TA spectroscopy was not used to study the photophysical processes [47].

Femtosecond transient spectra of **NI-PTZ-F-O** were also studied (Figure 6c, 6d). The solubility of **NI-PTZ-F-O** in HEX is poor, which leads to poor transient spectral signal (Figure S32c and S32d in Supporting Information File 1), we did not obtain the EADS, CS, CR, and other time constants exactly. In ACN, the first transient species (black line in Figure 6d) can be recognized as a localized singlet excited state of ^{1}NI* by comparison with the spectra reported in parent NI [58]. Within about 178 fs, the blue line which has two sharp peaks at 430 nm and 530 nm and a wide peak at 600−750 nm, this indicates that the beginning of ^{1}CS state formation. Then within 9.67 ps, there is a vibrational relaxation of the charge separated (CS) state. Later in about 4.53 ns, the triplet features of ^{3}LE appeared, with a characteristic absorption peak of ^{3}NI* at 463 nm. And this process can be ascribed to SOCT-ISC. This postulate is supported by the nanosecond transient spectra (see later section).

Nanosecond transient absorption (ns-TA) spectra

In order to study the lowest-lying transient species of the dyads formed upon photoexcitation, the ns-TA spectra of the **NI-PTZ-F** were studied (Figure 7a) in HEX. Upon pulsed laser excitation, a positive absorption band centered at ca. 430 nm was observed, which is inconsistent with the characteristic triplet state absorption of the NI unit (460 nm) [39], while this positive absorption band is closer to that of $NI^{-\bullet}$, which was determined at ca. 430 nm [58]. Therefore, this absorption band is assigned to the $NI^{-\bullet}$ radical anion. The excited state absorption (ESA) band centered at 460 nm is attributed to ^{3}NI state. Moreover, another positive absorption band centered at ca. 510 nm is attributed to absorption of $PTZ^{+\bullet}$ [39]. Therefore, we propose that the lowest T_1

state of **NI-PTZ-F** is admixture of ^{3}CS and ^{3}LE states. This is in agreement with the fs-TA spectral studies (Figure 6a, b). Similar ns-TA spectra was observed in other dyads without the PTZ unit oxidized (Figure S33 in Supporting Information File 1).

In order to study the solvent-dependency of the dyads contain native PTZ unit, the ns-TA spectra of **NI-PTZ-F** in solvents of HEX, TOL, DCM and ACN were studied (Figure 7). With increasing of the solvent polarity, the CS state energy will decrease, yet the ^{3}LE state energy will be intact to large extent [58]. The results showed that in HEX, both ^{3}LE and CS states were observed. Herein we assign the CS state to ^{3}CS, not ^{1}CS, based on lifetimes. Note even the ^{1}CS state (emission state) is populated via rISC, it is unlikely to be detected in ns-TA spectra due to its transient character (the lifetime of this state is short, its concentration is too low to be detected by the ns-TA spectra)

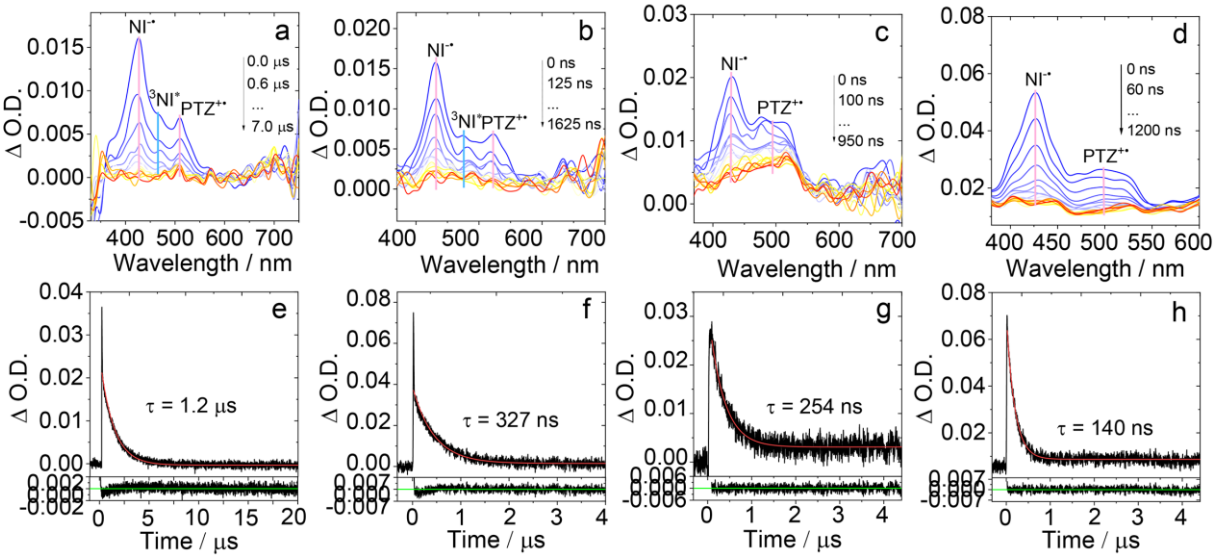

Figure 7: Nanosecond transient absorption spectra of **NI-PTZ-F** in (a) HEX (c = 2.0 × 10^{-5} M); (b) TOL (c = 2.0 × 10^{-5} M); (c) DCM (c = 1.0 × 10^{-4} M) and (d) ACN (c = 1.0 × 10^{-4} M). The corresponding decay traces are (e) HEX (c = 2.0 × 10^{-5} M); (f) TOL (c = 2.0 × 10^{-5} M); (g) DCM (c = 1.0 × 10^{-4} M) and (h) ACN (c = 1.0 × 10^{-4} M) at 430 nm. λ_{ex} = 355 nm, 20 °C.

[67,68]. The mono exponential decay kinetics indicate that the ^{3}LE and ^{3}CS state are in good equilibrium, i.e., the spin vibronic coupling, which is critical for the TADF [27,28,31,33,46].

In polar solvent, however, the ^{3}NI state signal in the ns-TA spectra diminished, but the $NI^{-\bullet}$ and $PTZ^{+\bullet}$ signals were persistent (Figure 7b, 7c and 7d). Moreover, the transient species lifetimes decreased to 140 ns in ACN. In polar solvents, the CS state energy become lower, therefore, only the ^{3}CS state was observed. In this case, we assume the spin vibronic coupling becomes weaker, accordingly, no TADF is resulted, even the ^{3}CS state is populated. Similar results were found for other unoxidized compounds (Figure S34 in Supporting Information File 1). Theoretical model predicts that without

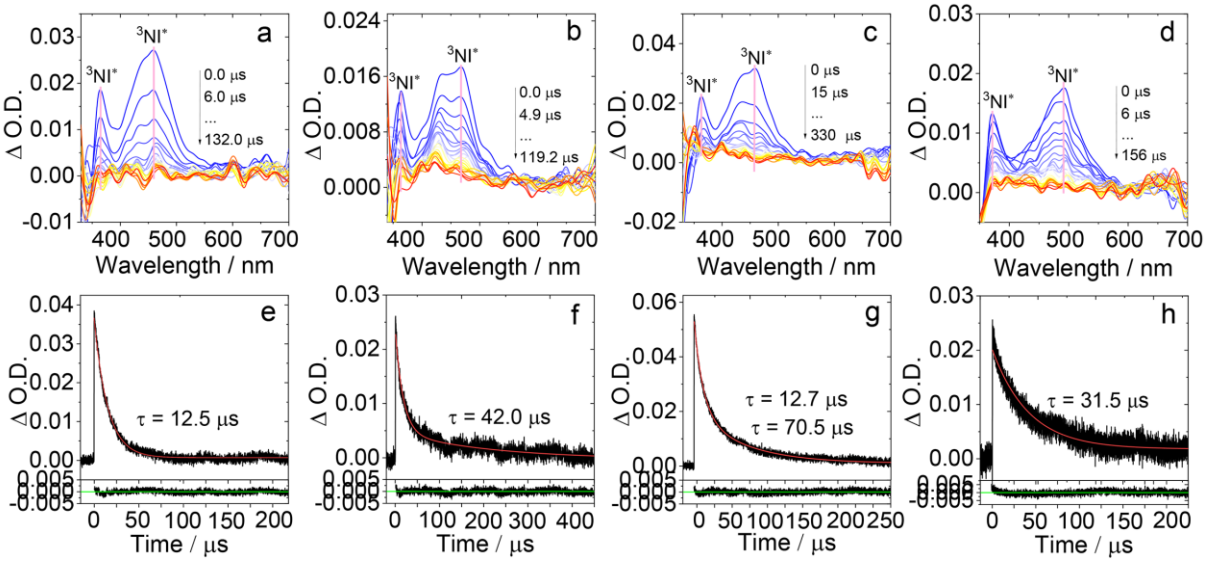

Figure 8: Nanosecond transient absorption spectra of (a) **NI-PTZ-F-O** (c = 4.0 × 10^{-5} M); (b) **NI-PTZ-Ph-O** (c = 4.0 × 10^{-5} M); (c) **NI-PTZ-C$_5$-O** (c = 4.0 × 10^{-5} M) and (d) **F-NI-Br** (c = 2.0 × 10^{-5} M). The corresponding decay traces are (e) **NI-PTZ-F-O** (c = 4.0 × 10^{-5} M); (f) **NI-PTZ-Ph-O** (c = 4.0 × 10^{-5} M); (g) **NI-PTZ-C$_5$-O** (c = 4.0 × 10^{-5} M) and (h) **F-NI-Br** (c = 2.0 × 10^{-5} M) in deaerated ACN at 460 nm. λ_{ex} = 355 nm, 20 °C.

the spin vibronic coupling, the rISC is non-efficient and the TADF will be inhibited [27,28,46]. Therefore, our results represent solid experimental evidence for the spin vibronic coupling model of the TADF.

The ns-TA spectra of oxidized molecules also were studied (Figure S35 in Supporting Information File 1) in HEX. For **NI-PTZ-F-O**, the ESA bands centered at 360 nm and 460 nm, were observed, which is attributed to ^{3}NI state. Moreover, the ESA bands are similar to the **F-NI-Br** and NI-Br [39]. Therefore, we propose that the low T_1 state of **NI-PTZ-F-O** is ^{3}LE state. Similar results were found for other oxidized molecules. With the increasing of the solvent polarity, the CS state energy decreases. Therefore, the ns-TA spectra of the compounds were studied (Figure 8) in ACN. We found that the transient absorption feature of the dyads with PTZ unit oxidized does not change, i.e., ^{3}LE state was observed even in ACN. This is supported by the ns-TA spectra of the reference compounds in ACN. Experimentally, no TADF was observed for these dyads. These results confirmed the critical role of the spin-vibronic coupling, i.e., ^{3}LE mediate ^{3}CS $\rightarrow$ ^{1}CS rISC in TADF [27].

Computational investigations

The optimized ground state geometry of the dyads at DFT-B3LYP/6-31G (d) level with Gaussian 09 shows that the dihedral angles between the PTZ and NI moieties are close to 90°, which is beneficial to SOCT-ISC (Figure 9). Thus, the ^{1}LE $\rightarrow$ ^{1}CS $\rightarrow$ ^{3}LE $\rightarrow$ ^{3}CS is facilitated, as well as the rISC processes, i.e., ^{3}CS $\rightarrow$ ^{3}LE $\rightarrow$ ^{1}CS, thus the TADF becomes possible. Moreover, we found the PTZ unit in the dyads adopt a puckered geometry (i.e., non-planer geometry). This is known for PTZ moiety [69,70]. We also optimized the geometry of the dyads at S_1 and T_1 states (Table S1 and S2 in supporting information File 1). In vacuum or non-polar solvents, the dihedral angles

between the NI and the PTZ moiety are in the range of 73–90 °, close to that at S_0 state. However, the PTZ unit adopt planar geometry, especially for the S_1 and T_1 state optimized in polar solvents. It is known that the $PTZ^{+\bullet}$ radical adopt a planer geometry [69,70]. These results indicates that the S_1 and T_1 states of the dyads containing native PTZ unit are CS state. For the dyads containing oxidized PTZ moiety, however, the PTZ moiety always adopt puckered geometry, indicating the S_1 and T_1 states of these dyads are LE stats, not CS state. These results infer that the T_1 state of the dyads with the PTZ oxidized is ^{3}LE state, not a ^{3}CS state, even in polar solvents, such as ACN. These results are supported by the ns-TA spectral observations.

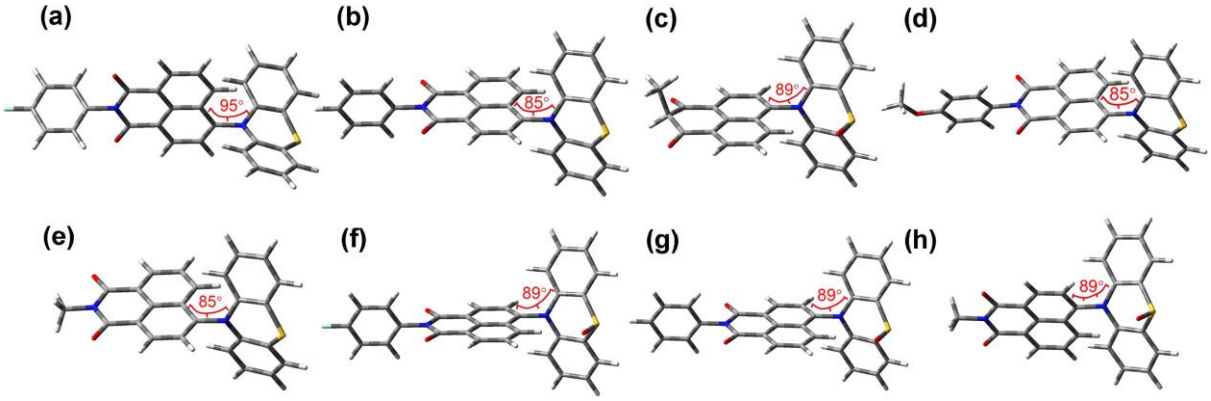

Figure 9: Optimized ground state geometry of (a) **NI-PTZ-F**; (b) **NI-PTZ-Ph**; (c) **NI-PTZ-CH_3**; (d) **NI-PTZ-OCH_3**, (e) **NI-PTZ-C_5**, (f) **NI-PTZ-F-O**; (g) **NI-PTZ-Ph-O** and (h) **NI-PTZ-C_5-O**. Calculated at the B3LYP/6-31G(d) level with Gaussian 09.

The spin density surface of the T_1 state of the dyads were computed (Figure 10 and Table S3 in Supporting Information File 1). For the dyads containing native PTZ moiety, the T_1 state density are delocalized on NI and PTZ moiety. Since these two moieties have different T_1 state energy (2.25 and 2.45 eV, respectively), the T_1 state should be a ^{3}CS state, not a ^{3}PTZ/^{3}NI states equilibrium. In polar solvents (e.g. ACN), literally the

same results were observed. These results are in agreement with the ns-TA spectral studies (Figure 7, Figure S33 and Figure S34 in Supporting Information File 1). For the dyads containing oxidized PTZ moieties, however, the T_1 state is always confined on the NI moiety. These results infer that the T_1 state of the dyads with the PTZ oxidized is ^{3}LE state, not a ^{3}CS state, even in polar solvents, such as ACN. These results are fully supported by the ns-TA spectral observations (Figure 8 and Figure S35 in Supporting Information File 1).

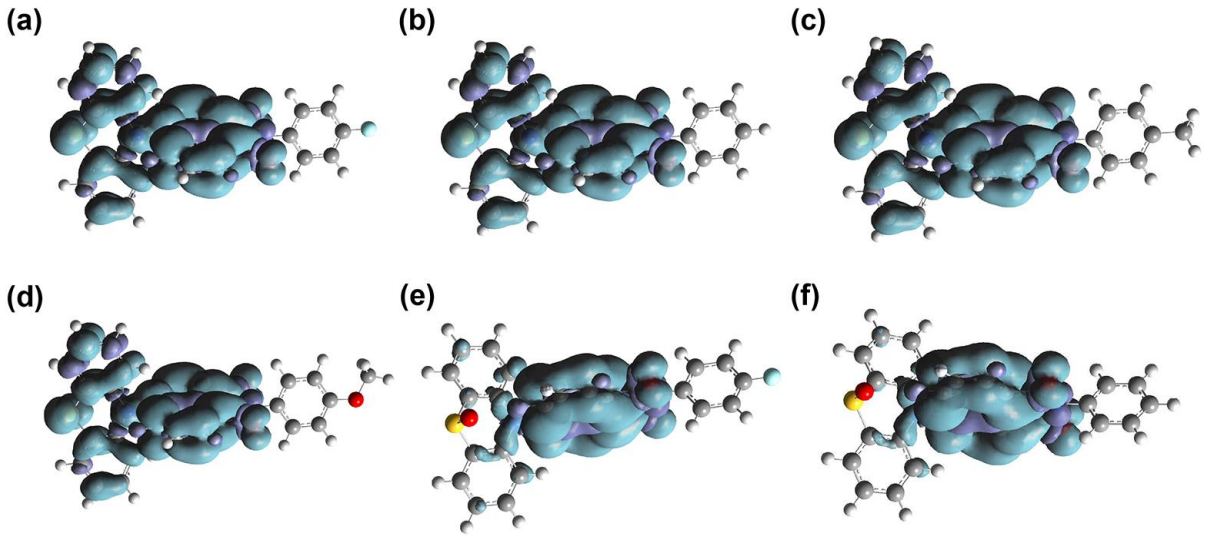

Figure 10: Spin density surfaces of the dyads at T_1 state (gas phase) of (a) **NI-PTZ-F**; (b) **NI-PTZ-Ph**; (c) **NI-PTZ-CH$_3$**; (d) **NI-PTZ-OCH$_3$**; (e) **NI-PTZ-F-O**; (f) **NI-PTZ-Ph-O**. Calculated at the B3LYP/6-31G(d) level with Gaussian 09. Isovalues = 0.02.

The frontier molecular orbitals (MOs) were studied (Figure 11 and Figure S36 in Supporting Information File 1). For all the dyads, the HOMOs are confined on the PTZ or the oxidized PTZ moieties, whereas the LUMOs are localized on the NI moieties. Interestingly, for the dyads containing native PTZ moiety, the HOMO energy is slightly varied by up to 0.04 eV, which is attributed to the electron withdrawal or donating

feature of the arylamine attached on the NI moieties. Interesting, although there is no distribution of LUMO on the arylamine moiety, the LUMO energy of the dyads are varied by up to 0.12 eV. These subtle variations of the molecular orbital energy impose effect on the photophysical property of the dyads. Such as the delayed fluorescence lifetime of the TADF emissions. Interestingly, upon oxidation of the PTZ moiety in the dyads, the HOMO energy decreases substantially, by up to 0.8 eV, whereas the LUMO energy changed by less than 0.2 eV, thus, the energy gap of HOMO/LUMO increases upon oxidation of the PTZ moiety. This is supported by the blue-shifted fluorescence of the dyads with the PTZ moieties oxidized as compared to the dyads containing the

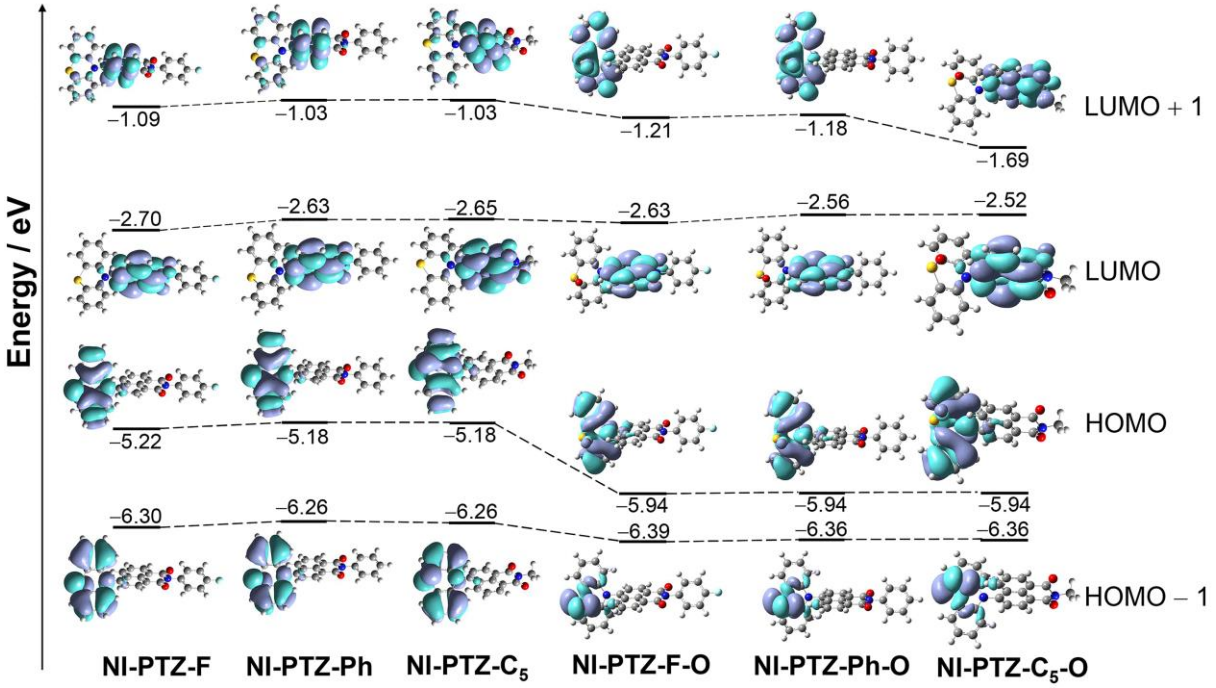

Figure 11: Selected frontier molecular orbitals of **NI-PTZ-F**; **NI-PTZ-Ph**; **NI-PTZ-C$_5$**; **NI-PTZ-F-O**; **NI-PTZ-Ph-O** and **NI-PTZ-C$_5$-O** calculated by DFT at the B3LYP/6-31G(d) level with Gaussian 09W, based on the optimized ground state geometries, respectively. Isovalues = 0.02.

native PTZ moiety (Figure 2). Since the NI moiety is intact, thus the ^{3}CS state becomes much higher than the ^{3}LE state, we postulate the TADF will vanish for these dyads. This conclusion is fully supported by the experimental observations. These studies show that our strategy of tuning the energy ordering of the ^{1}CS, ^{3}LE and ^{3}CS states by changing the electron donating and withdrawal capability of the PTZ and NI moieties is successful.

The photophysical processes of the dyads are summarized in Scheme 2. For **NI-PTZ-F**, the ^{1}CS, ^{3}CS and ^{3}LE states share similar energy. Thus, TADF was observed. The efficient spin-vibronic coupling of the ^{3}CS/^{3}LE states was supported by ns-TA spectral studies, in which both the ^{3}CS and ^{3}LE states were observed, and the two transient species decay with the same kinetics. In polar solvents, however, the CS state energy decreases sharply, yet, the ^{3}LE state energy does not change, thus, although a long-lived ^{3}CS state was observed in ACN (τ_{CS} = 140 ns), no TADF was observed. This is solid experimental evidence that spin-vibronic coupling is essential for TADF, and the ^{3}CS $\rightarrow$ ^{1}CS rISC is slow, without the coupling with the intermediate ^{3}LE state. The conventionally used transient luminescence spectral method is unable to supply such in-depth mechanistic insights to the TADF mechanism. For the dyads with the PTZ unit oxidized, however, the CS state energy is increased by up to 0.8 eV, yet the ^{3}LE state energy does not change, thus the spin-vibronic coupling between the ^{3}LE and ^{3}CS is weak, no TADF was observed for this dyad, only a long-live ^{3}LE state was observed with the ns-TA spectra. These studies are useful for study of the complicated photophysical processes involved in the TADF of electron donor-acceptor dyads, and for molecular structure design of new electron donor-acceptor TADF emitters.

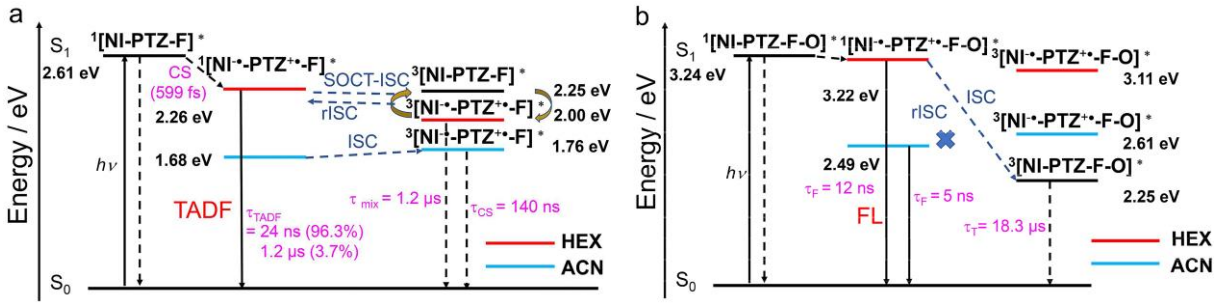

Scheme 2: Simplified Jablonski diagram of (a) **NI-PTZ-F** and (b) **NI-PTZ-F-O**. The ^{1}LE state (^{1}[NI-PTZ-F-O]*) energy is derived from the spectroscopic data (the intersection of normalized UV–vis absorption and fluorescence spectra); The triplet state (^{3}[NI$^{-\bullet}$-PTZ$^{+\bullet}$-F-O]*) energy is computed by TDDFT method, which were performed at the B3LYP/6-31G(d) level with Gaussian 09W; The ^{1}CT state (^{1}[NI$^{-\bullet}$-PTZ$^{+\bullet}$-F-O]*) energy is obtained from electrochemical data in Table 4 (^{1}CS/^{3}CS: $2J < 0.2$ eV).

Conclusions

In summary, we prepared a series of naphthalimide (NI)-phenothiazine (PTZ) electron donor-acceptor dyads, to make an in-depth study of the photophysical mechanism of the thermally activated delayed fluorescence (TADF) of the electron donor-acceptor emitters. In order to tune the photophysical properties, we change the electron donating and the electron withdrawal capability of the PTZ and NI moieties, respectively. From the UV–vis absorption and fluorescence emission spectra, we observed the changing of charge transfer (CT) absorption bands, which showed the tuning effect. For the dyads containing native PTZ unit, TADF was observed, and with the changing of different arylamine, the prompt and delayed fluorescence lifetimes changed as while. In polar solvent, no TADF was observed. Moreover, we did not observe TADF in the dyads with the PTZ unit oxidized. Femtosecond transient absorption spectra show the charge separation takes ca. 0.6 ps, and formation of the admixture of ^{3}LE and ^{1}CS/^{3}CS state was observed (in *n*-hexane). The decay of the ^{1}CS

state and CR in aerated *n*-hexane take ca. 7.92 ns. While for the dyads with PTZ unit oxidized, ^{1}CS state formation takes ca. 178 fs and the charge recombination takes 4.53 ns to given ^{3}LE state (in acetonitrile). Nanosecond transient absorption (ns-TA) spectra show that both ^{3}CS and ^{3}LE states were observed for the scenario where TADF occur, whereas only ^{3}LE state or the ^{3}CS state was observed for the systems lacking of TADF. This is a rare but unambiguous experimental evidence that the spin-vibronic coupling of ^{3}CS/^{3}LE states is crucial for TADF. Without the mediating effect of the ^{3}LE state, no TADF will be resulted, even the long-lived ^{3}CS state is populated (lifetime $\tau_{CS} \approx 140$ ns). This experimental result confirms the $^3\text{CS} \rightarrow {}^1\text{CS}$ rISC is slow, without coupling with an approximate ^{3}LE state. These studies are useful for in-depth understanding of the photophysical mechanisms of the TADF emitters, as well as for molecular structure design of new electron donor-acceptor TADF emitters.

Experimental section

General method

All the chemicals used in synthesis are analytical pure and were used as received without purification. UV–vis absorption spectra were measured on a UV-2550 Shimadzu spectrophotometer. Fluorescence spectra were recorded with an FS5 spectrofluorometer (Edinburgh instruments Ltd., U.K.). Fluorescence quantum yields (Φ_F) were measured by absolute photoluminescence quantum yield spectrometer (Quantaurus-QY Plus C13534-11, Hamamatsu Ltd., Japan). Luminescence lifetimes of compounds were measured with an OB920 luminescence lifetime spectrometer (Edinburgh Instruments Ltd., U.K.). **NI-PTZ-F**; **NI-PTZ-Ph**; **NI-PTZ-CH$_3$**; **NI-PTZ-OCH$_3$**;

and the oxidized molecules **NI-PTZ-F-O** were prepared according to the literature methods [11,39,43,71].

Synthesis of NI-PTZ-F

Compound **NI-PTZ-F** was synthesized by a modified literature method [39]. Under N_2 atmosphere, **F-NI-Br** (200 mg, 0.542 mmol), phenothiazine (130 mg, 0.650 mmol), $Pd(OAc)_2$ (22 mg, 0.098 mmol) and sodium *tert*-butoxide (70 mg, 0.732 mmol) were dissolved in dry toluene (8 mL). Then tri-*tert*-butylphosphine tetrafluoroborate (19 mg, 0.065 mmol) was added. The mixture was refluxed and stirred for 8 h under N_2. After cooling, water (20 mL) was added, and the mixture was extracted with ethyl acetate (3 $\times$ 30 mL). The combined organic layer was separated and washed with water and brine (3 $\times$ 30 mL), respectively. The combined organic layer was dried over anhydrous Na_2SO_4 and the solvent was evaporated under reduced pressure. The crude product was purified by column chromatography (silica gel, DCM:PE = 1:5, v:v). Compound **NI-PTZ-F** was obtained as orange solid. Yield: 40 mg (15%). M.p.: 136.2–137.2 °C. ^{1}H NMR ($CDCl_3$, 400 MHz) δ: 8.87 (d, J = 7.63 Hz, 1H), 8.70 (d, J = 7.25 Hz, 1H), 8.60 (d, J = 8.51 Hz, 1H), 8.00 (d, J = 7.63 Hz, 1H), 7.77–7.81 (m, 1H), 7.29–7.35 (m, 4H), 7.11 (d, J = 7.51 Hz, 2H), 6.85–6.88 (m, 2H), 6.77–6.80 (m, 2H), 6.08 (d, J = 8.13 Hz, 2H). ^{13}C NMR ($CDCl_3$, 125 MHz) δ: 162.94, 158.14, 151.94, 142.63, 138.20, 138.16, 130.82, 130.32, 127.96, 127.63, 124.62, 123.54, 121.12, 117.50, 116.43, 111.80. HRMS (ESI, *m*/*z*) calcd for $C_{30}H_{17}FN_2O_2S$ $[M+H]^+$, 489.0995, found 489.1072.

Synthesis of NI-PTZ-Ph

NI-PTZ-Ph was synthesized was synthesized with a method similar to that of **NI-PTZ-F**, and it has been reported [11,71]. The crude product was purified by column chromatography (silica gel, DCM:PE = 1:3, v:v). Compound **NI-PTZ-Ph** was obtained

as orange solid. Yield: 243 mg (52%). M.p.: 126.2–127.2 °C. ^{1}H NMR ($CDCl_3$, 400 MHz) δ: 8.87 (d, J = 7.63 Hz, 1H), 8.70 (d, J = 7.13 Hz, 1H), 8.59 (d, J = 8.38 Hz, 1H), 7.99 (d, J = 7.63 Hz, 1H), 7.76–7.80 (m, 1H), 7.57–7.61 (m, 2H), 7.52 (d, J = 7.38 Hz, 1H), 7.35 (d, J = 7.25 Hz, 2H), 7.11 (d, J = 7.50 Hz, 2H), 6.77–6.87 (m, 4H), 6.09 (d, J = 7.76 Hz, 2H). HRMS (ESI, m/z) calcd for $C_{30}H_{18}N_2O_2S$ $[M+H]^+$, 471.1089, found 471.1159.

Synthesis of NI-PTZ-CH$_3$

NI-PTZ-CH$_3$ was synthesized with a method similar to that of **NI-PTZ-F**. The crude product was purified by column chromatography (silica gel, DCM:PE = 1:3, v:v). The product was obtained as orange solid. Yield: 230 mg (80%). M.p.: 100.2–101.5 °C. ^{1}H NMR ($CDCl_3$, 400 MHz) δ: 8.87 (d, J = 7.63 Hz, 1H), 8.69 (d, J = 8.38 Hz, 1H), 8.58 (d, J = 8.50 Hz, 1H), 7.98 (d, J = 7.76 Hz, 1H), 7.75–7.79 (m, 1H), 7.38 (d, J = 8.01 Hz, 2H), 7.23 (d, J = 8.26 Hz, 2H), 7.10 (dd, J_1 = 1.50 Hz, J_2 = 1.50 Hz, 2H), 6.84–6.88 (m, 2H), 6.78–6.80 (m, 2H), 6.08 (dd, J_1 = 1.13 Hz, J_2 = 1.13 Hz, 2H), 2.46 (s, 3H). ^{13}C NMR ($CDCl_3$, 125 MHz) δ: 164.10, 163.73, 143.67, 138.78, 132.45, 132.17, 131.36, 130.55, 130.35, 130.19, 128.29, 127.13, 123.27, 120.61, 115.83, 21.32. HRMS (ESI, m/z) calcd for $C_{31}H_{20}N_2O_2S$ $[M+H]^+$, 485.1245, found 485.1325.

Synthesis of NI-PTZ-OCH$_3$

NI-PTZ-OCH$_3$ was synthesized with a method similar to that of **NI-PTZ-F**. The crude product was purified by column chromatography (silica gel, DCM:PE = 1:5, v:v). The product was obtained as orange solid. Yield: 55 mg (22%). M.p.: 123.2–124.3 °C. ^{1}H NMR ($CDCl_3$, 400 MHz) δ: 8.87 (d, J = 7.63 Hz, 1H), 8.70 (d, J = 7.25 Hz, 1H), 8.58 (d, J = 8.51 Hz, 1H), 7.98 (d, J = 7.63 Hz, 1H), 7.75–7.79 (m, 1H), 7.27 (s, 1H), 7.25 (s, 1H), 7.08–7.12 (m, 4H), 6.76–6.87 (m, 4H), 6.08 (d, J = 8.13 Hz, 2H), 3.89 (s, 3H). ^{13}C

NMR ($CDCl_3$, 125 MHz) δ: 164.03, 163.66, 143.74, 143.40, 132.21, 131.39, 130.43, 129.46, 128.86, 128.63, 128.33, 127.13, 127.07, 123.29, 120.61, 115.83, 56.13. HRMS (ESI, *m*/*z*) calcd for $C_{31}H_{20}N_2O_3S$ $[M+H]^+$, 501.1195, found 501.1276.

Synthesis of NI-PTZ-F-O

Compound **NI-PTZ-F-O** was synthesized by a modified literature method [43]. Compound **NI-PTZ-F** (36 mg, 0.074 mmol) was dissolved in glacial acetic acid (5 mL), H_2O_2 (1.5 mL, 30%, 1.184 mmol) was added dropwise. The mixture was stirred at 40 °C for 4 h. The reaction mixture was poured into water and the pH of the mixture was brought to 7 with a saturated aqueous solution of Na_2CO_3. After cooling, water (10 mL) was added, and the mixture was extracted with ethyl acetate (20 mL × 3). The organic layer was separated and washed with water and brine solution (20 mL × 3), respectively. The combined organic layers were dried over anhydrous Na_2SO_4 and the solvent was evaporated under reduced pressure. The crude product was purified by column chromatography (silica gel, DCM:MeOH = 50:1, v:v) and was obtained as yellow solid. Yield: 28 mg (76%). M.p.: 100.1–101.0 °C. ^{1}H NMR ($CDCl_3$, 400 MHz) δ: 8.87 (d, *J* = 7.63 Hz, 1H), 8.70 (d, *J* = 7.26 Hz, 1H), 8.59 (d, *J* = 7.26 Hz, 1H), 8.00 (d, *J* = 7.26 Hz, 1H), 7.76–7.80 (m, 1H), 7.30 (d, *J* = 8.26 Hz, 4H), 7.11 (d, *J* = 7.51 Hz, 2H), 6.85–6.88 (m, 2H), 6.78–6.80 (m, 2H), 6.50 (d, *J* = 7.51 Hz, 2H). ^{13}C NMR ($CDCl_3$, 125 MHz) δ: 163.73, 163.36, 140.89, 140.32, 133.24, 133.05, 132.01, 130.62, 130.40, 130.31, 123.79, 123.62, 123.05, 116.81, 116.72, 116.49. HRMS (MALDI, *m*/*z*) calcd for $C_{30}H_{17}FN_2O_3S$ $[M+H]^+$, 505.0944, found 505.0973.

Electrochemical Studies

The cyclic voltammetry curves were recorded with CHI610D electrochemical workstation (CHI instruments, Inc., Shanghai, China). In a N_2 purged saturated

solutions containing 0.10 M Bu_4NPF_6 as a supporting electrolyte; counter electrode is platinum electrode; glassy carbon electrode is working electrode; and the $Ag/AgNO_3$ (0.1 M in ACN) couple as the reference electrode. Ferrocenium/ferrocene (Fc^+/Fc) redox couple was used as an internal reference.

Femtosecond Transient Absorption Spectroscopy.

Femtosecond transient absorption spectra (fs-TA) were acquired on a system based on a Ti: sapphire regenerative amplifier (Coherent Astrella). The system produces 40 fs pulses at 800 nm, with a repetition rate of 1 kHz. The instrument resolution is 100 fs. Excitation pulses at 340 nm were produced by a commercial parametric amplifier. The pump beam polarization has been set to the magic angle with respect to the probe beam. The probe beam has been obtained by focusing a small portion of the fundamental 800 nm beam on a 2 mm CaF_2 crystal, kept under continuous rotation to avoid damage. The pump-probe delay has been introduced by sending the portion of the fundamental beam used for white light generation through a motorized translator. After focusing and overlapping the pump and probe beams at the sample position, the probe beam has been directed through a spectrograph and to the detector. The sample was contained in a 1 mm quartz cuvette mounted on a movable stage, in order to avoid photo-decomposition. The data were subdivided in two different time intervals and fitted using the Glotaran-Application 1.5.1 and Surface Xplorer software. The number of kinetic components to be used for Global analysis has been estimated by performing a preliminary singular values decomposition (SVD) analysis. All data were chirp-corrected before global fitting.

Nanosecond Transient Absorption Spectroscopy.

The nanosecond transient absorption spectra were measured on a LP920 laser flash photolysis spectrometer (Edinburgh Instruments, Ltd., U.K.). The data (kinetic decay

traces and the transient difference absorption spectra) were analyzed with the L900 software. All samples were deaerated with N_2 for ca. 15 min before measurement, and excited with a nanosecond pulsed laser (OPO nanosecond pulsed laser). The wavelength is tunable in the range of 410−2500 nm.

Calculation study

The geometries of the compounds in their ground state were optimized using Density Functional Theory (DFT) with B3LYP functional and 6-31G(d) basis set [72]. The excited states geometries of S_1 and T_1 were optimized with time-dependent TD-DFT (DFT) using the same functional and basis sets as in the ground state optimizations [73]. The spin density of the compounds were optimized using DFT with the B3LYP functional and 6-31G(d) basis set. The excitation energy of the compounds was calculated by TD-DFT at B3LYP/6-31G(d) level.

Supporting Information

General experimental methods, ^{1}H NMR, ^{13}C NMR, HRMS spectra of the compounds, theoretical computation data and the photophysical data. [https://www.beilstein-journals.org/bjoc/content/ supplementary/xxxxx.pdf]

Funding

J.Z. thanks the NSFC (U2001222), the Research and Innovation Team Project of Dalian University of Technology (DUT2022TB10), the Fundamental Research Funds for the Central Universities (DUT22LAB610) and the State Key Laboratory of Fine Chemicals for financial support. X.Z. thanks the support of the "Fundamental Research Funds for the Central Universities".

References

1. Yersin, H.; *Highly efficient OLEDs with phosphorescent materials*; John Wiley & Sons: Hoboken, USA, 2008.
2. Uoyama, H.; Goushi, K.; Shizu, K.; Nomura, H.; Adachi, C. *Nature* **2012**, *492*, 234–238. doi: 10.1038/nature11687
3. Wong, M. Y.; Zysman-Colman, E. *Adv. Mater.* **2017**, *29*, 1605444. doi: 10.1002/adma.201605444
4. Bui, T.-T.; Goubard, F.; Ibrahim-Ouali, M.; Gigmes, D.; Dumur, F. *Beilstein J. Org. Chem.* **2018**, *14*, 282–308. doi: 10.3762/bjoc.14.18
5. Huang, T.; Jiang, W.; Duan, L. *J. Mater. Chem. C* **2018**, *6*, 5577–5596. doi: 10.1039/C8TC01139G
6. Cai, X.; Su, S.-J. *Adv. Funct. Mater.* **2018**, *28*, 1802558. doi: 10.1002/adfm.201802558
7. Ni, F.; Li, N.; Zhan, L.; Yang, C. *Adv. Opt. Mater* **2020**, *8*, 1902187. doi: 10.1002/adom.201902187
8. Chen, X.-K. *CCS Chem.* **2020**, *2*, 1256–1267. doi: 10.31635/ccschem. 020.202000281
9. Xu, Y.; Xu, P.; Hu, D.; Ma, Y. *Chem. Soc. Rev.* **2021**, *50*, 1030–1069. doi: 10.1039/D0CS00391C
10. Shi, Y.-Z.; Wu, H.; Wang, K.; Yu, J.; Ou, X.-M.; Zhang, X.-H. *Chem. Sci.* **2022**, *13*, 3625–3651. doi: 10.1039/D1SC07180G
11. Wu, Y.; Thermally-activated delayed fluorescence red light materials containing naphthalimide structure, synthesis method and application. CN. Pantent 11, 5, 57228, 8, January 6, 2023
12. Guo, Y.; Gao, Y.; Zhang, J.; Wang, C.; Wang, Y.; Feng, X.; Zhao, G. *J. Phys. Chem. C* **2023**, *127*, 4784–4791. doi: 10.1021/acs.jpcc.2c08920
13. Dias, F. B.; Penfold, T. J.; Monkman, A. P. *Methods Appl. Fluoresc.* **2017**, *5*, 012001. doi: 10.1088/2050-6120/aa537e
14. Hou, Y.; Zhang, X.; Chen, K.; Liu, D.; Wang, Z.; Liu, Q.; Zhao, J.; Barbon, A. *J. Mater. Chem. C* **2019**, *7*, 12048–12074. doi: 10.1039/C9TC04285G
15. Filatov, M. A. *Org. Biomol. Chem.* **2020**, *18*, 10–27. doi: 10.1039/C9OB02170A

16. Gibbons, D. J.; Farawar, A.; Mazzella, P.; Leroy-Lhez, S.; Williams, R. M. *Photochem. Photobiol. Sci.* **2020**, *19*, 136–158. doi: 10.1039/c9pp00399a
17. Bassan, E.; Gualandi, A.; Cozzi, P. G.; Ceroni, P. *Chem. Sci.* **2021**, *12*, 6607–6628. doi: 10.1039/D1SC00732G
18. Zhang, X.; Wang, Z.; Hou, Y.; Yan, Y.; Zhao, J.; Dick, B. *J. Mater. Chem. C* **2021**, *9*, 11944–11973. doi: 10.1039/D1TC02535J
19. Cui, L.-S.; Gillett, A. J.; Zhang, S.-F.; Ye, H.; Liu, Y.; Chen, X.-K.; Lin, Z.-S.; Evans, E. W.; Myers, W. K.; Ronson, T. K.; Nakanotani, H.; Reineke, S.; Bredas, J.-L.; Adachi, C.; Friend, R. H. *Nat. Photonics* **2020**, *14*, 636–642. doi: 10.1038/s41566-020-0668-z
20. Lv, L.; Yuan, K.; Zhao, T.; Wang, Y. *J. Mater. Chem. C* **2020**, *8*, 10369–10381. doi: 10.1039/D0TC02235G
21. Wang, L.; Ou, Q.; Peng, Q.; Shuai, Z. *J. Phys. Chem. A* **2021**, *125*, 1468–1475. doi: 10.1021/acs.jpca.0c09767
22. Tanaka, H.; Shizu, K.; Miyazaki, H.; Adachi, C. *Chem. Commun.* **2012**, *48*, 11392–11394. doi: 10.1039/C2CC36237F
23. Tanaka, H.; Shizu, K.; Nakanotani, H.; Adachi, C. *J. Phys. Chem. C* **2014**, *118*, 15985–15994. doi: 10.1021/jp501017f
24. Penfold, T. J. *J. Phys. Chem. C* **2015**, *119*, 13535–13544. doi: 10.1021/acs.jpcc.5b03530
25. Peng, Q.; Fan, D.; Duan, R.; Yi, Y.; Niu, Y.; Wang, D.; Shuai, Z. *J. Phys. Chem. C* **2017**, *121*, 13448–13456. doi: 10.1021/acs.jpcc.7b00692
26. Li, X.; Shen, S.; Zhang, C.; Liu, M.; Lu, J.; Zhu, L. *Sci China Chem* **2021**, *64*, 534–546. doi: 10.1007/s11426-020-9908-5
27. Gibson, J.; Monkman, A. P.; Penfold, T. J. *ChemPhysChem* **2016**, *17*, 2956–2961. doi: 10.1002/cphc.201600662
28. Etherington, M. K.; Gibson, J.; Higginbotham, H. F.; Penfold, T. J.; Monkman, A. P. *Nat. Commun.* **2016**, *7*, 13680. doi: 10.1038/ncomms13680
29. Samanta, P. K.; Kim, D.; Coropceanu, V.; Brédas, J.-L. *J. Am. Chem. Soc.* **2017**, *139*, 4042–4051. doi: 10.1021/jacs.6b12124
30. Kim, I.; Jeon, S. O.; Jeong, D.; Choi, H.; Son, W.-J.; Kim, D.; Rhee, Y. M.; Lee, H. S. *J. Chem. Theory Comput* **2020**, *16*, 621–632. doi: 10.1021/acs.jctc.9b01014

31. Lin, S.; Pei, Z.; Zhang, B.; Ma, H.; Liang, W. *J. Phys. Chem. A* **2022**, *126*, 239–248. doi: 10.1021/acs.jpca.1c08456
32. Ward, J. S.; Nobuyasu, R. S.; Batsanov, A. S.; Data, P.; Monkman, A. P.; Dias, F. B.; Bryce, M. R. *Chem. Commun.* **2016**, *52*, 2612–2615. doi: 10.1039/C5CC09645F
33. Evans, E. W.; Olivier, Y.; Puttisong, Y.; Myers, W. K.; Hele, T. J. H.; Menke, S. M.; Thomas, T. H.; Credgington, D.; Beljonne, D.; Friend, R. H.; Greenham, N. C. *J. Phys. Chem. Lett.* **2018**, *9*, 4053–4058. doi: 10.1021/acs.jpclett.8b01556
34. Hosokai, T.; Matsuzaki, H.; Nakanotani, H.; Tokumaru, K.; Tsutsui, T.; Furube, A.; Nasu, K.; Nomura, H.; Yahiro, M.; Adachi, C. *Sci. Adv.* **2017**, *3*, e1603282. doi: 10.1126/sciadv.1603282
35. Choi, J.; Ahn, D.-S.; Oang, K. Y.; Cho, D. W.; Ihee, H. *J. Phys. Chem. C* **2017**, *121*, 24317–24323. doi: 10.1021/acs.jpcc.7b07553
36. Freeman, D. M. E.; Musser, A. J.; Frost, J. M.; Stern, H. L.; Forster, A. K.; Fallon, K. J.; Rapidis, A. G.; Cacialli, F.; McCulloch, I.; Clarke, T. M.; Friend, R. H.; Bronstein, H. *J. Am. Chem. Soc.* **2017**, *139*, 11073–11080. doi: 10.1021/jacs.7b03327
37. Noda, H.; Chen, X.-K.; Nakanotani, H.; Hosokai, T.; Miyajima, M.; Notsuka, N.; Kashima, Y.; Brédas, J.-L.; Adachi, C. *Nat. Mater.* **2019**, *18*, 1084–1090. doi: 10.1038/s41563-019-0465-6
38. Hosokai, T.; Matsuzaki, H.; Furube, A.; Tokumaru, K.; Tsutsui, T.; Nakanotani, H.; Yahiro, M.; Adachi, C. *Dig. Tech. Pap. - Soc. Inf. Disp. Int. Symp.* **2016**, *47*, 786–789. doi: 10.1002/sdtp.10790
39. Tang, G.; Sukhanov, A. A.; Zhao, J.; Yang, W.; Wang, Z.; Liu, Q.; Voronkova, V. K.; Di Donato, M.; Escudero, D.; Jacquemin, D. *J. Phys. Chem. C* **2019**, *123*, 30171–30186. doi: 10.1021/acs.jpcc.9b09335
40. Vázquez, R. J.; Yun, J. H.; Muthike, A. K.; Howell, M.; Kim, H.; Madu, I. K.; Kim, T.; Zimmerman, P.; Lee, J. Y.; Goodson, T., III *J. Am. Chem. Soc.* **2020**, *142*, 8074–8079. doi: 10.1021/jacs.0c01225
41. Fisher, L., Jr.; Vázquez, R. J.; Howell, M.; Muthike, A. K.; Orr, M. E.; Jiang, H.; Dodgen, B.; Lee, D. R.; Lee, J. Y.; Zimmerman, P.; Goodson, T., III *Chem. Mater.* **2022**, *34*, 2161–2175. doi: 10.1021/acs.chemmater.1c03668
42. Zhao, X.; Zhao, J. *Chem. Commun.* **2022**, *58*, 7666–7669. doi: 10.1039/D2CC01958B

43. Zhao, X.; Sukhanov, A. A.; Jiang, X.; Zhao, J.; Voronkova, V. K. *J. Phys. Chem. Lett.* **2022**, *13*, 2533−2539. doi: 10.1021/acs.jpclett.2c00435
44. Zhang, X.; Zhao, X.; Ye, K.; Zhao, J. *Chem. Eur. J.* **2023**, *29*, e202203737. doi: 10.1002/chem.202203737
45. Ogiwara, T.; Wakikawa, Y.; Ikoma, T. *J. Phys. Chem. A* **2015**, *119*, 3415−3418. doi: 10.1021/acs.jpca.5b02253
46. Drummond, B. H.; Aizawa, N.; Zhang, Y.; Myers, W. K.; Xiong, Y.; Cooper, M. W.; Barlow, S.; Gu, Q.; Weiss, L. R.; Gillett, A. J.; Credgington, D.; Pu, Y.-J.; Marder, S. R.; Evans, E. W. *Nat. Commun.* **2021**, *12*, 4532. doi: 10.1038/s41467-021-24612-9
47. Ye, K.; Cao, L.; van Raamsdonk, D. M. E.; Wang, Z.; Zhao, J.; Escudero, D.; Jacquemin, D. *Beilstein J. Org. Chem.* **2022,** *18,* 1435**–**1453. doi:10.3762/bjoc.18.149
48. Chen, K.; Yang, W.; Wang, Z.; Iagatti, A.; Bussotti, L.; Foggi, P.; Ji, W.; Zhao, J.; Di Donato, M. *J. Phys. Chem. A* **2017**, *121*, 7550−7564. doi: 10.1021/acs.jpca.7b07623
49. Imran, M.; El-Zohry, A. M.; Matt, C.; Taddei, M.; Doria, S.; Bussotti, L.; Foggi, P.; Zhao, J.; Di Donato, M.; Mohammed, O. F.; Weber, S. *J. Mater. Chem. C* **2020**, *8*, 8305−8319. doi: 10.1039/D0TC00017E
50. dos Santos, P. L.; Etherington, M. K.; Monkman, A. P. *J. Mater. Chem. C* **2018**, *6*, 4842−4853. doi: 10.1039/C8TC00991K
51. Kaputskaya, I. A.; Ermilov, E. A.; Tannert, S.; Röder, B.; Gorbatsevich, S. K. *J. Lumin.* **2006**, *121*, 75−87. doi: 10.1016/j.jlumin.2005.10.005
52. Wang, Z.; Zhao, J.; Di Donato, M.; Mazzone, G. *Chem. Commun.* **2019**, *55*, 1510−1513. doi: 10.1039/C8CC08159J
53. Hou, Y.; Liu, J.; Zhang, N.; Zhao, J. *J. Phys. Chem. A* **2020**, *124*, 9360−9374. doi: 10.1021/acs.jpca.0c07907
54. Dong, Y.; Elmali, A.; Zhao, J.; Dick, B.; Karatay, A. *ChemPhysChem* **2020**, *21*, 1388−1401. doi: 10.1002/cphc.202000300
55. Sasaki, S.; Hattori, K.; Igawa, K.; Konishi, G.-i. *J. Phys. Chem. A* **2015**, *119*, 4898−4906. doi: 10.1021/acs.jpca.5b03238
56. Lakowitz J. *Principles of Fluorescence Spectroscopy*; Kluwer Academic Publishers: Dordrecht, The Netherlands, 1999.

57. Rout, Y.; Montanari, C.; Pasciucco, E.; Misra, R.; Carlotti, B. *J. Am. Chem. Soc.* **2021**, *143*, 9933–9943. doi: 10.1021/jacs.1c04173

58. Zhang, X.; Liu, X.; Taddei, M.; Bussotti, L.; Kurganskii, I.; Li, M.; Jiang, X.; Xing, L.; Ji, S.; Huo, Y.; Zhao, J.; Di Donato, M.; Wan, Y.; Zhao, Z.; Fedin, M. V. *Chem. Eur. J.* **2022**, *28*, e202200510. doi: 10.1002/chem.202200510

59. Tian, W.; Sukhanov, A. A.; Bussotti, L.; Pang, J.; Zhao, J.; Voronkova, V. K.; Di Donato, M.; Li, M.-D. *J. Phys. Chem. B* **2022**, *126*, 4364–4378. doi: 10.1021/acs.jpcb.2c02276

60. Niu, X.; Tajima, K.; Kong, J.; Tao, M.; Fukui, N.; Kuang, Z.; Shinokubo, H.; Xia, A. *Phys. Chem. Chem. Phys.* **2022**, *24*, 14007–14015. doi: 10.1039/D2CP00295G

61. Chen, X.; Pang, J.; Imran, M.; Li, X.; Zhao, J.; Li, M. *Photochem. Photobiol. Sci.* **2021**, *20*, 69–85. doi: 10.1007/s43630-020-00002-w

62. Schuster, D. I.; Cheng, P.; Jarowski, P. D.; Guldi, D. M.; Luo, C.; Echegoyen, L.; Pyo, S.; Holzwarth, A. R.; Braslavsky, S. E.; Williams, R. M.; Klihm, G. *J. Am. Chem. Soc.* **2004**, *126*, 7257–7270. doi: 10.1021/ja038676s

63. Ziessel, R.; Allen, B. D.; Rewinska, D. B.; Harriman, A. *Chem. Eur. J.* **2009**, *15*, 7382–7393. doi: 10.1002/chem.200900440

64. Karimata, A.; Kawauchi, H.; Suzuki, S.; Kozaki, M.; Ikeda, N.; Keyaki, K.; Nozaki, K.; Akiyama, K.; Okada, K. *Chem. Lett.* **2013**, *42*, 794–796. doi: 10.1246/cl.130062

65. Ventura, B.; Bertocco, A.; Braga, D.; Catalano, L.; d'Agostino, S.; Grepioni, F.; Taddei, P. *J. Phys. Chem. C* **2014**, *118*, 18646–18658. doi: 10.1021/jp5049309

66. Gifford, L. A.; Miller, J. N.; Phillipps, D. L.; Burns, D. T.; Bridges, J. W. *Anal. Chem.* **1975**, *47*, 1699–1702. doi: 10.1021/ac60359a061

67. Tyson, D. S.; Henbest, K. B.; Bialecki, J.; Castellano, F. N. *J. Phys. Chem. A* **2001**, *105*, 8154–8161. doi: 10.1021/jp011770f

68. Zhang, X.; Hou, Y.; Xiao, X.; Chen, X.; Hu, M.; Geng, X.; Wang, Z.; Zhao, J. *Coord. Chem. Rev.* **2020**, *417*, 213371. doi: 10.1016/j.ccr.2020.213371

69. Okamoto, T.; Kuratsu, M.; Kozaki, M.; Hirotsu, K.; Ichimura, A.; Matsushita, T.; Okada, K. *Org. Lett.* **2004**, *6*, 3493–3496. doi: 10.1021/ol048698z69

70. Singhabhandhu, A.; Robinson, P. D.; Fang, J. H.; Geiger, W. E. *Inorg. Chem.* **1975**, *14*, 318–323. doi: org/10.1021/ic50144a022

71. Wang, B.; Zheng, Y.; Wang, T.; Ma, D.; Wang, Q. *Org. Electron.* **2021**, *88*, 106012. doi: org/10.1016/j.orgel.2020.106012

72. Yanai, T.; Tew, D. P.; Handy, N. C. *Chem. Phys. Lett.* **2004**, *393*, 51–57. doi: 10.1016/j.cplett.2004.06.011
73. Hirata, S.; Head-Gordon, M. *Chem. Phys. Lett.* **1999**, *314*, 291–299. doi: 10.1016/S0009-2614(99)01149-5